Revealing Transport, Dissolution, and Precipitation Behaviors in Electrokinetic-Geochemical Reaction System at Pore-to-Core Scales

Tang, Kunning; Su, Hongli; Bo, Zhenkai; Da Wang, Ying; Mostaghimi, Peyman; Armstrong, Ryan T.

Important note
To cite this publication, please use the final published version (if applicable).
Please check the document version above.

Kunning Tang and Hongli Su contributed equally to this work.

Key Points:

- A new core-scale experiment and pore-scale time-lapse imaging are used to understand mineral dissolution and precipitation
- Uniform ion transport and mineral dissolution are observed, with modeling using pore-scale data showing a high correlation to experiments
- Four mineral dissolution and three secondary precipitation patterns are identified during the electrokinetic reactive transport process

Revealing Transport, Dissolution, and Precipitation Behaviors in Electrokinetic-Geochemical Reaction System at Pore-to-Core Scales

Kunning Tang[1] , Hongli Su[2], Zhenkai Bo[3], Ying Da Wang[1], Peyman Mostaghimi[4] , and Ryan T. Armstrong[4]

[1]School of Minerals and Energy Resources Engineering, University of New South Wales, Sydney, NSW, Australia, [2]Department of Engineering Structures, Faculty of Civil Engineering and Geosciences, Resource & Recycling, Delft University of Technology, Delft, The Netherlands, [3]Institute of GeoEnergy Engineering, Heriot-Watt University, Edinburgh, UK, [4]School of Civil and Environmental Engineering, University of New South Wales, Sydney, NSW, Australia

Abstract Net-zero carbon targets drive the development of new underground activities such as hydrogen storage and in situ critical mineral recovery, all of which involve geochemical reactions between minerals and fluid/ion transport. Understanding these processes is key to optimizing efficiency and minimizing environmental impacts. However, the fundamental mechanisms of ion transport, mineral dissolution, and secondary precipitation remain poorly understood, particularly at the pore scale. This gap partly arises from the challenges of characterizing samples at such a fine scale, where fluid/ion transport and reactions occur simultaneously. Herein, a core-to-pore-scale experimental approach, combined with time-lapse three-dimensional (3D) imaging, is designed to characterize fluid/ion transport, dissolution, and precipitation processes. We implemented this workflow in an electrokinetic in situ recovery (EK-ISR) system. Time-lapse 3D micro-computed tomography (micro-CT) images were acquired during the experiment to observe dissolution and precipitation dynamics and to measure pore-scale physical parameters. Findings indicate uniform reactive ion transport and mineral dissolution under EK conditions, with over 78% of the target mineral dissolved. Time-lapse images reveal multiple dissolution and precipitation patterns that influence reactive transport processes. Geochemical modeling based on pore-scale parameters demonstrates over 90% correlation with core-scale experimental data. Our workflow demonstrates a promising capability for characterizing reactive transport processes across pore-to-core scales.

Plain Language Summary New subsurface activities like hydrogen storage and in situ recovery of critical minerals are being developed for non-zero carbon targets. These subsurface processes involve fluid flow, ion transport, and mineral reactions, and understanding these reactions is essential to improving efficiency and reducing environmental harm. However, the detailed mechanisms of how ions move, minerals dissolve, and new minerals form, especially at small scales, are not well understood. We designed an experimental and imaging approach that connects core-scale and pore-scale observations to study these processes. Using 3D micro-CT imaging, we observed how minerals dissolved and precipitated within the sample at several time steps. Our results show that reactive ions are uniformly transported into the sample and react with minerals under external voltage. We also identified different types of dissolution and precipitation during the process. We then used these pore-scale quantifications as input to a geochemical model. The output is closely matched with core-scale experimental data. This approach offers a promising way to better understand and characterize these important geochemical processes.

1. Introduction

For decades, underground anthropogenic activities have primarily focused on resource extraction, such as oil/gas production and mineral recovery from open-pit and underground mining (Ben-Awuah et al., 2016; Holditch, 2013; Maitland, 2000; Xiaoguang et al., 2018). Recently, with the implementation of net-zero carbon policies, numerous underground climate solutions have been proposed, incorporating various strategies and technologies aiming to reduce carbon emissions, replace traditional processes with more environmentally friendly practices, and promote sustainability. These solutions include carbon capture and sequestration (CCS), underground hydrogen storage (UHS), EK (electrokinetic) remediation, ISR (in situ recovery) or EK-ISR (Hellerschmied et al., 2024; Karami et al., 2021; Krevor et al., 2023; Seredkin et al., 2016; Tarkowski, 2019; Wang

et al., 2023). All these solutions involve varying degrees of interaction with subsurface minerals. These interactions often result in mineral dissolution and precipitation, which are critical factors influencing the effectiveness of these activities (Bo et al., 2021; Kumar et al., 2023; Martens et al., 2021a; Menefee et al., 2017). For example, in UHS, reactive minerals such as calcite or pyrite can undergo dissolution and precipitation under specific conditions, causing mechanical or microbial risks (Al-Yaseri et al., 2024). Similarly, in ISR, a lixiviant is directly injected into the orebody to dissolve and recover metal minerals. This process can lead to the precipitation of secondary minerals (Dutrizac, 1990; Kanakiya et al., 2017), which reduces the reactive surface area of the target mineral and can block pore throats, thereby decreasing recovery efficiency (Martens et al., 2021a). Therefore, a comprehensive understanding of mineral dissolution and precipitation processes is essential for optimizing these technologies and minimizing their long-term impacts on the environment.

Subsurface mineral dissolution and precipitation are the results of geochemical reactions in subsurface gas-brine-rock systems (when applicable) (Qin et al., 2023). During anthropogenic injection of exogenous fluids (or production) into the subsurface, molecular activities increase or decrease, breaking the equilibrium and changing the mineral saturation index (SI) (Bo et al., 2021). As a result, the mineral dissolves when SI is lower than 0 and precipitates when SI is greater than 0. In this context, geochemical reaction and reactive transport modeling coupled with experimental investigation are heavily conducted to study and characterize the mineral dissolution and precipitation in various earth and environmental processes (Menefee et al., 2017; Steefel, 2019). From the depiction of the hydrodynamic status of a multi-component natural solution to the prediction of hydrogen loss due to microbial activities during UHS cyclic operation (Tremosa et al., 2023), geochemical reactions modeling has facilitated the applications of the latest underground climate solutions such as CCS (Awolayo et al., 2022) and UHS (Shojaee et al., 2024) in a more complex system (Steefel, 2019). These models often consider the dissolution and precipitation of carbonate and sandstone minerals, processes that occur over decades or even geological time scales (Zeng et al., 2022). In contrast, for metal mineral recovery, minerals such as chalcopyrite and pyrite have dissolution rate laws measured in hours (Y. Li et al., 2015), and their sulfide solutes pose significant environmental risks (Salomons, 1995). However, geochemical reaction models for subsurface mineral recovery, such as ISR and EK-ISR, are not as well understood as those for UHS or CCS, despite their potential to solve the negative environmental impacts of conventional mineral recovery processes (Wang et al., 2022).

ISR refers to the process of extracting minerals from underground without excavation. A lixiviant is injected into the ore body, dissolves the target minerals, and then pumped back to the surface for processing (Seredkin et al., 2016). This technique has been used widely for uranium leaching and potentially extends to copper and gold extraction (Kuhar et al., 2018; Mudd, 2001; Sinclair & Thompson, 2015). EK-ISR is an emerging technology that enhances the recovery of minerals by applying an electric field to the subsurface ore body. Its field scale process is shown in Figure 1a. Charged ions are transported under electrical force to the target minerals, where metal ions are dissolved and moved toward the electrode (Tang et al., 2024). Compared to traditional ISR, which uses hydraulic pressure to pump lixiviant, EK-ISR, although still in its proof-of-concept stage, shows several potential advantages: uniform transport into ore bodies, particularly effective in heterogeneous formations, reduced chemical usage, limited spread of contaminants to groundwater, and lower energy consumption (Martens et al., 2021a; Tang, Li, et al., 2023; Wang et al., 2022). Investigating the process at the multiscale is beneficial to enhancing our understanding of the mechanisms behind the EK-ISR. Figure 1b shows the multiscale analysis of EK-ISR from the pore scale, core scale, pilot scale, and the largest field scale, respectively. Current analysis of EK-ISR mainly focused on the core scale to pilot scale (Karami et al., 2023; Martens et al., 2021b; Wang et al., 2023). Given that EK-ISR contains complex physicochemical mechanisms, such as ion transport within porous media, mineral dissolution processes, and secondary precipitation phenomena (Figure 1c), it is essential to investigate these fundamental mechanisms at the pore scale.

Mineral dissolution and precipitation are commonly modeled through transition state rate theory (TST) (Lasaga, 1981) where the rate law is given by (Steefel et al., 2015)

$$R_m = \text{sgn}[\Omega] A_m k_m \left(\prod a^n \right) \left| \exp\left(\frac{\eta \Delta G}{RT} \right) - 1 \right|^m \tag{1}$$

where $\text{sgn}[\Omega]$ indicates the sign of the reaction term (negative for dissolution, positive for precipitation), A_m represents the reactive surface area of the reacting mineral, k_m is the rate constant, and the term $\prod a^n$ accounts for
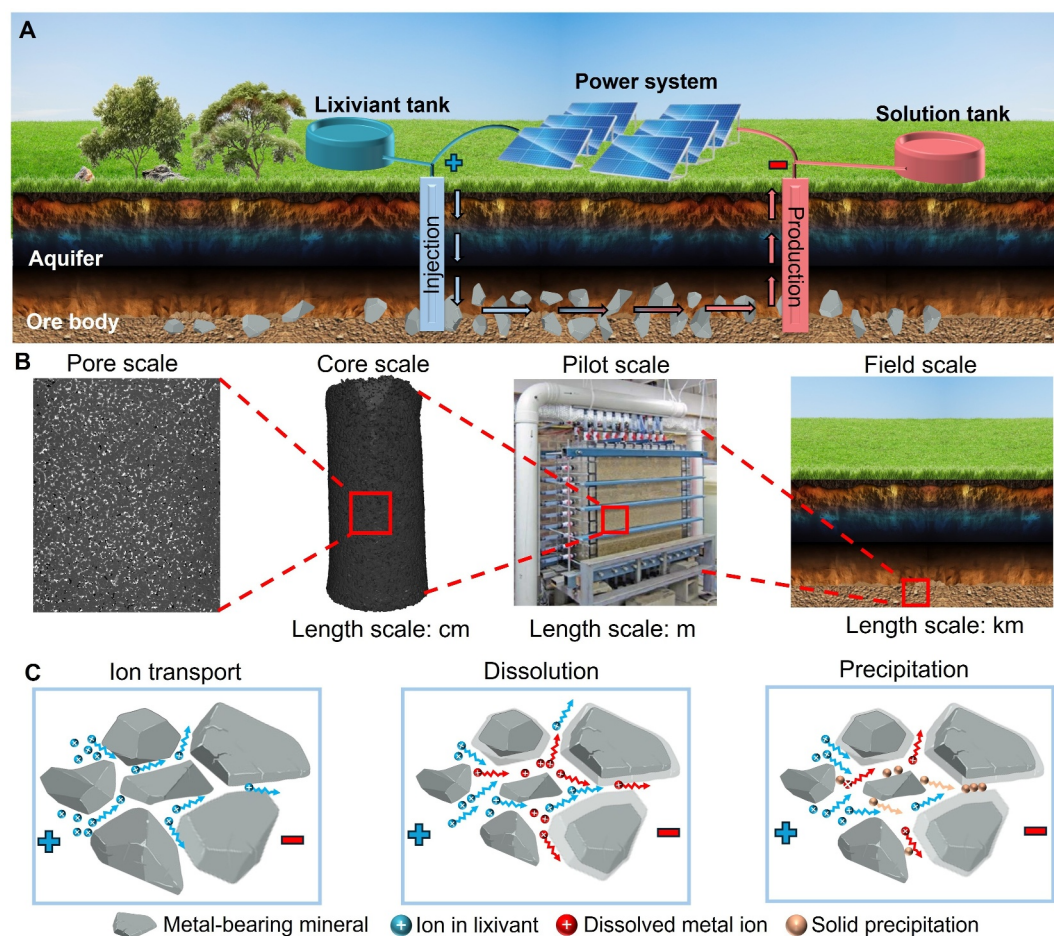
Figure 1. (a) 3D illustration of EK-ISR at field scale. (b) EK-ISR process from small to large scale, including pore scale, core scale, pilot scale, and field scale. (c) Illustration of the fundamental mechanisms in EK-ISR at the pore scale, including ion transport in porous media, mineral dissolution, and precipitation.

all far-from-equilibrium effects on the reaction, which may be catalytic or inhibitory (assuming a zero exponent if there is no effect on the reaction rate). The parameters η and m are experimentally or theoretically determined exponents, and ΔG is the thermodynamic driving force of the reaction. From Equation 1, one can find that mineral dissolution and precipitation are affected by various factors such as temperature, pH, brine salinity, mineral reactive surface area, etc (Qin et al., 2023). Several dedicated databases have been developed and recognized for modeling reaction kinetics of a wide variety of minerals based on TST (Marty et al., 2015; Palandri & Kharaka, 2004; Zhang et al., 2019), while the choice of mineral reactive surface area varies significantly (Bo et al., 2021; Martens et al., 2021a; Menefee et al., 2017; Zeng et al., 2022). This variability arises because, in the context of geochemical reactions in porous media, the mineral reactive surface area can change as the reaction progresses, a process that is not yet fully understood. (Qin et al., 2023), especially in the emerging fields such as UHS or EK-ISR (Bo et al., 2021; Khajooie et al., 2024; Martens et al., 2021a). In contrast, substantial research has been conducted on the evolution of reactive surface area during CCS. For example, (Beckingham et al., 2016) calculated mineral surface area from the two-dimensional (2D) registered image by computing the perimeter of each discrete mineral grain in the 2D scanning electron microscopy (SEM) image and shows a better match with experimental effluent data compared to a conventional Brunauer-Emmett-Teller (BET) measurement. Their method heavily relies on the 2D SEM images for mineral accessibility, which is then multiplied by the 3D connected surface area (from 3D X-ray CT images) to calculate the accessible specific surface area (SSA) of a mineral (Awolayo et al., 2022; Qin et al., 2023). However, analyzing mineral grains in 2D, which are intrinsically 3D, leads to sampling errors, stereological effects, and inaccurate estimates of geochemical properties such as
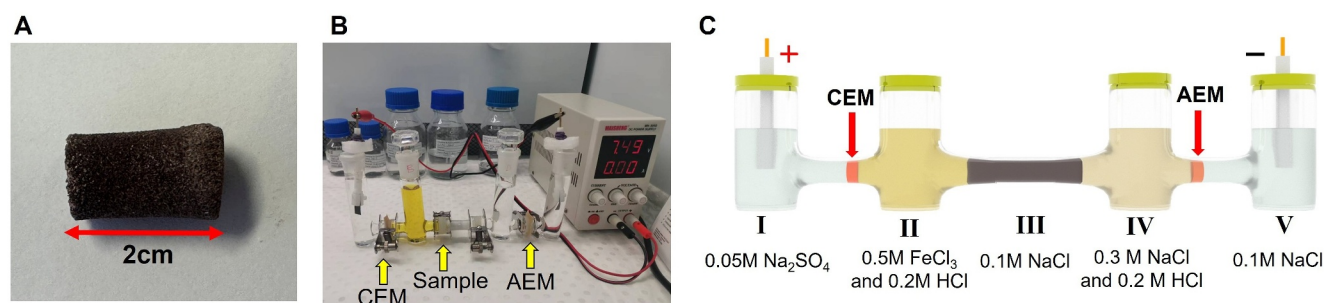
Figure 2. Visualization of (a) Consolidated chalcopyrite sample used in the experiment, (b) Experimental setup, and (c) Schematic of the experimental setup.

SSA (Tang et al., 2022). Moreover, the unique evolution of each mineral grain during dissolution and precipitation will be ignored as all these grains are treated as one single phase in the sample (Qin et al., 2023).

From the literature, one can conclude that ion transport, mineral dissolution, and precipitation are the primary reactive transport processes influencing underground activities, particularly crucial for mineral recovery processes such as EK-ISR. Therefore, we present a comprehensive experimental and 3D image-based workflow to investigate the fundamental aspects of ion transport, metal mineral dissolution, and secondary precipitation relevant to the EK-ISR process. We begin by creating a consolidated sample composed of chalcopyrite (a primary copper-bearing mineral) and glass beads. This sample helps us better understand fundamental geochemical behaviors of mineral dissolution and precipitation, in contrast to real ore samples with complex mineralogy and high uncertainty in results. An EK copper extraction experiment is conducted under an electric field, with the sample being scanned three times during the recovery using 3D micro-computed tomography (micro-CT). Leaching conditions, including pH, voltage, and concentrations, can be experimentally quantified. Meanwhile, chalcopyrite dissolution and secondary precipitation can be qualitatively visualized and quantitatively characterized in 3D using time-lapse micro-CT images. Each chalcopyrite grain can be isolated and characterized as an individual instance. This allows for the quantification of geochemical parameters such as SSA, chalcopyrite-lixiviant contact, and the mass and volume of chalcopyrite on a per-grain basis and their variation at different recovery stages at the pore scale. A direct diffusion simulation is conducted on the 3D images to characterize the changes in tortuosity and the connectivity of pathways associated with the reactive transport processes. Finally, a Phreeqc model is developed based on widely used chalcopyrite dissolution rate laws (Kimball et al., 2010) and our 3D image-based mineral fluid-accessible specific surface areas to validate our mineral characterization results through grain-wise and core-scale dissolution predictions.

2. Materials and Methods

2.1. Experimental Procedure

2.1.1. Experimental Preparation

Chemicals and materials used in the study are summarized in this section. Hydrochloric acid (HCl, 37%), sodium hydroxide (NaOH), ferric chloride (FeCl$_3$), sodium chloride (NaCl), and sodium sulfate (Na$_2$SO$_4$) are purchased from Sigma-Aldrich, Australia. All chemicals are of analytical grade and used as received. Deionized (DI) water with a resistivity of $\sim 1.6 \times 10^{-4}$ s/m is prepared by a Milli-Q ultrapure water purification system (Merck). Chalcopyrite (>80 µm) is purchased from Kremer Pigmente GMbH & Co.KG, Germany. Three sizes of soda-lime glass beads (90 ~ 150 µm, 100 ~ 200 µm, 150 ~ 250 µm) are purchased from LabFiend, Australia. Platinum (Pt) electrodes, rubber rings, and the glass setup are purchased from a local market, Sydney, Australia. Cation exchange membrane (CEM, CXM-200S) and anion exchange membrane (AEM, AXM-100S) are purchased from Membranes International Inc., USA.

The consolidated chalcopyrite sample (Figure 2a) is made by mixing 1.8 g of glass beads of three sizes (0.6 g each) with 0.2 g of chalcopyrite. The mixture of glass beads and chalcopyrite is sintered in a graphite mold composed of three sections. The middle section of the mold has a pre-drilled void with a diameter of 1 cm and a length of 2 cm to hold the mixture. The mold containing the mixture is gradually moved into a furnace preheated to a temperature of 700 °C (exceeding the melting point of glass beads but lower than the melting point of

chalcopyrite). During this process, nitrogen is slowly injected to displace the oxygen, which prevents both the expansion of the graphite plate and the oxidation of the beads. Under these conditions, the glass beads gradually melt, binding the entire mixture into a consolidated sample with a diameter of 8 mm and a length of 2 cm. The entire heating process takes approximately 20 min. After the furnacing process, the fabricated sample is placed vertically inside a glass tube. Water droplets are then poured onto the top of the sample to determine whether they pass through and exit from the bottom, confirming that the fabricated sample functions as a percolating column.

The component analysis of chalcopyrite powders is analyzed by X-ray diffraction (XRD, X'pert Powder, PANalytical Empyrean, UK) and X-ray fluorescence (XRF, M4 TORNADO, Bruker, USA) spectroscopy. We first analyzed the XRF to confirm the elements existing in the chalcopyrite powder. After that, we perform XRD analysis on the chalcopyrite. The chalcopyrite powder is prepared as a random powder by the back-loading method. The powder is measured by PANalytical Empyrean with a Co tube instrument. HighScore Plus software was used for XRD data processing. The ICSD database was used to search candidate crystalline phases for mineral phase identification. A Rietveld fit is performed with HighScore Plus software for quantitative estimation of individual phases. Mineral phase identification is confirmed by matching peak intensities with the ICSD database and further validated through elemental analysis via XRF. The mineral phase analysis result from XRD can be found in Figure S1 in Supporting Information S1. Solutions in reservoirs II and IV are periodically sampled during the experiments, and the concentration of Fe and Cu is quantified by the Inductively Coupled Plasma-Mass Spectrometer (ICP-MS, Nexion5000, PerkinElmer, USA). The pH values in reservoirs (I, II, IV, and V) are recorded at the same time via a calibrated electrode (PHS-3C, Hangzhou Qiwei Instrument Co., Ltd., China).

2.1.2. Experimental Setup and Procedure

A core-scale setup is constructed for investigating mineral dissolution and precipitation using EK (Figures 2b and 2c) (Martens et al., 2021a). It consists of five reservoirs, representing the anode (I), source (II), core holding (III), target (IV), and cathode (V) reservoirs, respectively. Reservoirs are clamped together with rubber rings to avoid fluid leakage. Pt electrodes are placed in reservoirs I and V, connecting with a DC power supplier at a constant voltage of 7.5 V. With this, a constant electric field exists across every reservoir.

Reservoir I contains 20 mL of Na_2SO_4 solution (0.05 M) as the anolyte, while reservoir II contains 20 mL of the lixiviant solution consisting of 0.5 M $FeCl_3$ in 0.2 M HCl (Antonijević & Bogdanović, 2004; Bennett et al., 2012; Hiroyoshi et al., 2002; Martens et al., 2021a). The chalcopyrite sample is saturated in a 0.1 M NaCl solution under vacuum for 2 days, followed by an additional 2 days at ambient pressure before being placed in reservoir III. Reservoir IV, containing 0.3 M NaCl in 0.2 M HCl (20 mL), works as the collecting tank. Reservoir V has NaCl (0.1 M, 20 mL) as the catholyte. CEM is added between reservoirs I and II. AEM is added between reservoirs IV and V. These membranes segregate the electrolytic solution from the remainder of the system, thereby restricting the ion transport in reservoirs II–IV. With the external DC power, cationic ions within the lixiviant (e.g., Fe^{3+} and H^+) migrate from reservoir II to IV via reservoir III. Similarly, leached Cu^{2+} follows the same direction. AEM prevents cationic ions from entering reservoir V, which will contaminate and corrode the Pt electrodes. The cationic ions are eventually collected in reservoir IV. However, water electrolysis occurs in reservoirs I and V under the applied external potential. To counterbalance the generation of hydrogen (H^+) and hydroxyl (OH^-) ions at the anode and cathode, respectively, Alkali (NaOH, 4 M) and acid (HCl, 4 M) solutions are periodically added to neutralize the electrolytes in reservoirs I and V, respectively. The NaCl-HCl solution in reservoir IV is renewed every 4 days to avoid precipitation generation due to the accumulation of cations. A 1 mL sample of the fluid is collected from reservoirs II and IV every 6 hr for ion measurement. pH values in reservoirs II and IV are also regularly measured. The whole experimental period is 1,200 hr. The summary of solutions used in each reservoir is listed in Table S1 in Supporting Information S1.

Chalcopyrite dissolution reaction in reservoir III by dissolved Fe^{3+} are described as (Antonijević & Bogdanović, 2004; Martens et al., 2021a):

$$CuFeS_2 + 4Fe^{3+} \rightarrow Cu^{2+} + 5Fe^{2+} + 2S^0 \qquad (2)$$
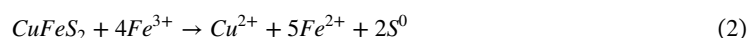
Where chalcopyrite ($CuFeS_2$) is reacted with Fe^{3+} and the dissolved. Aside from dissolution, elemental sulfur is produced during leaching (Dutrizac, 1990), which could then be precipitated in the sample.

2.2. Time-Lapse 3D Micro-CT Imaging and Processing

3D micro-CT images at three timesteps are taken during the EK-ISR experiments. These images offer valuable insights into the analysis of mineral dissolution and precipitation. The following section will provide details of time-lapse micro-CT image generation and post-processing methods.

2.2.1. Image Generation and Scanning Setting

Time-lapse micro-CT images are captured at three distinct stages: (a) the initial stage, before the experiment begins; (b) the middle stage, taken after 500 hr of experiment, and (c) the final stage, taken at the end of the experiment, after 1,200 hr. At the middle stage, we pause the experiment and carefully remove the sample from Reservoir III. The sample is then placed in DI water for 1 day to remove the inside reactive ions through the concentration gradient. Afterward, it is dried in the fume hood for two more days before conducting the second scan. Detailed parameter settings for the micro-CT scans are listed in Table S2 in Supporting Information S1. The scanned 3D images have a dimension of 2,119 × 2,113 × 4,066 voxels with a voxel resolution of 4 μm.

After acquiring three micro-CT images, pre-processing is performed, including image normalization and image registration. Image normalization is used to convert the 16-bit original micro-CT image into an 8-bit format, thereby reducing the redundant grayscale values and compressing the data to half its original size. Image registration is a necessary step since the sample has been scanned three times from different orientations. This process aligns the images from the initial, middle, and final stages to a common coordinate system and orientation. The registration process involves manually pre-aligning the same region from three images in the X-Y plane, followed by the use of the "Register Images" module in TM Avizo software to align the images in 3D space. In the "Register Images" module, we choose "Euclidean" as the similarity metric between the two images and "QuasiNewton" as the optimization strategy. After registration, the three images would have exactly the same orientation and dimension. This alignment enables an accurate comparison between these three images, allowing for analysis of change over time.

2.2.2. Multi-Phase Segmentation and Per-Grain/Pore Isolation

After registering these images, the next step is multi-phase segmentation, which clusters every voxel into different phases and enables further quantification. Using the watershed segmentation method (Beucher & Meyer, 2018), each image is segmented into three phases: the glass bead phase, the chalcopyrite phase, and the pore phase. This is performed in the TM Avizo software. Segmentation errors, such as small connected components and partial volume effects (PVE) at phase boundaries, are corrected using morphological processing techniques. This includes dilation and erosion to eliminate the PVE effect (Tang et al., 2022) and separating connected components to remove small connected components. Each grain and pore is then isolated sequentially from images at three stages using the "Separating objects" function in Avizo. Given that the original chalcopyrite grain size exceeds 80 μm, and with a voxel resolution of 4 μm, at least 20 voxels are required in each dimension to accurately represent a chalcopyrite grain. Consequently, we established a threshold value of 256, ensuring that any isolated grain with a total voxel count below 256 (equivalent to approximately 6–7 voxels in one direction, which is significantly smaller than the required 20 voxels) is classified as a segmentation error and is subsequently excluded. This process allows for a per-grain quantitative analysis, enabling the measurement of each chalcopyrite grain's dissolution pattern, including grain size and SSA variation (Tang, Da Wang, et al., 2023). The overall image processing workflow is shown in Figure 3.

2.3. Transport-Related Quantification

2.3.1. Ion Transport Regime

Understanding ion transport behavior under experimental conditions is crucial, as it offers insight into how reactive ions are transported and interact with target minerals. Ion transport regime under our EK-ISR experiment as a single-phase multi-component flow system can be characterized using two dimensionless numbers: the Advection Diffusion Index (ADI) and the Electrodiffusivity Index (EDI) (Tang et al., 2024). ADI represents the ratio of advective flux to diffusive flux, while EDI represents the ratio of electromigration flux to diffusive flux. Both terms can be estimated directly from the experiment using the following equations (Tang et al., 2024):
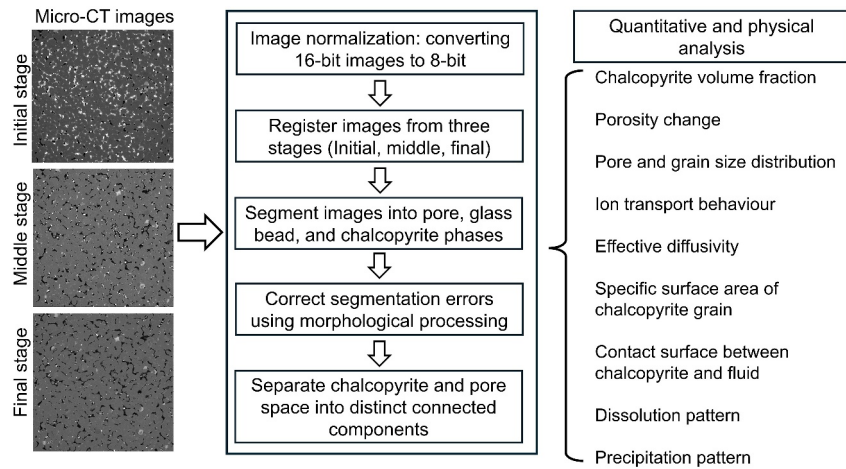
Figure 3. Overall workflow for processing time-lapse micro-CT images and a list of physical parameters derivable from the final processed outputs.

$$ADI = \frac{\boldsymbol{u}L\bar{C}_i}{-D_i(C_{i,in} - C_{i,out})} \tag{3}$$

and

$$EDI = \frac{z_i\psi\bar{C}_i}{V_T(C_{i,in} - C_{i,out})}. \tag{4}$$

Where $\boldsymbol{u}$ is the average fluid flow velocity, $\bar{C}_i$ is the average ith ion concentration through the system, D_i is the diffusivity of the ith ion, z_i is the ion algebraic valency, V_T is the thermal voltage which is defined as $V_T = k_B T/e$, where k_B is the Boltzmann constant, T is the temperature, and e is the electron charge, $C_{i,in}$ and $C_{i,out}$ are the concentration of ith ion at inlet and outlet, where L is the characteristic length, and ψ is the applied external electric potential.

2.3.2. Effective Diffusion Simulation

Diffusivity is a crucial parameter that governs the transport of substances through porous media, effectively characterizing the connectivity of pathways between the inlet and outlet. While core-flooding based methods for experimentally determining effective diffusivity for porous media exist Guo et al. (2022), we leverage the availability of resolved pore-space 3D images to digitally determine the effective diffusivity by solving an elliptic diffusion equation within the pore space of the 3D images (Chung et al., 2019). This calculation is performed on the image at all three stages. The conservation of mass can be represented as:

$$\nabla \cdot \vec{v} = q \tag{5}$$

where $\vec{v}$ is the diffusive velocity field, and q represents the source or sink term, which is assumed to be zero herein. A local diffusion coefficient D is assigned on each voxel, which relates the local diffusion velocity to the concentration gradient as:

$$\vec{v} = -D\nabla C \tag{6}$$

where C is the concentration. The value of D represents the diffusion coefficient of any given gas in air or solute in some solvent, that is, the diffusion coefficient in free, unobstructed space D. In order to generalize the effect of the porous structure on D such that a value of $D_{eff} < D$ can be determined, we assume that at relatively low concentrations, the tortuosity of the porous structure τ relates the parameters as $D_{eff} = \tau D$. This generalization

allows the calculation of tortuosity to be proportional to the effective diffusivity. In this study, we assign all pore voxels a value of $D = 1$ and all solid voxels $D = 0$.

Combining Equations 5 and 6 gives the Diffusion Equation:

$$-\nabla \cdot (D\nabla C) = 0 \tag{7}$$

This equation is solved using Two Point Flux Approximation (TPFA) (Sandve et al., 2012) and Finite Volume Methods with an Algebraic Multi-Grid (AMG) solver, applying prescribed constant concentration (Dirichlet) boundary conditions at the inlet $C = 1$ and outlet $C = 0$. All solid voxels are excluded from the system of equations, thereby reducing the system matrix. After calculating the spatial concentration distribution and diffusion velocity profile, the dimensionless effective diffusivity is estimated from:

$$D_{eff} = \frac{J_D N_x R}{\Delta C} \tag{8}$$

The length of the system is expressed as the number of voxels multiplied by the resolution of the image R, with each voxel (each grid block) spanning the image resolution. The number of voxels in the main flow direction is shown as N_z, J_D is the overall diffusion flow rate, ΔC is the concentration difference across the domain, imposed as boundary conditions.

2.4. Dissolution and Precipitation-Related Parameters Quantification

Based on the reaction equation in Equation 2, chalcopyrite is dissolved with the presence of Fe^{3+}, and elemental sulfur is precipitated. The following sections describe the physical parameters that are used to characterize dissolution and precipitation behaviors.

2.4.1. Basic Physical Characterization

The volume fractions of pores, chalcopyrite, and glass beads of the sample can be directly obtained from the segmented images at each stage. This is achieved by counting the voxels corresponding to each component and dividing by the total number of voxels.

At each stage, the mass of every chalcopyrite grain can be calculated from:

$$Mass_i = \frac{Mass_{init}}{N_{init}} \times N_i \tag{9}$$

where $Mass_i$ refers to the mass of ith chalcopyrite grain, $Mass_{init}$ refers to the total mass of chalcopyrite powder at initial stage, which is 0.2 g, N_{init} is the total number of voxels that are segmented as chalcopyrite at initial stage, and N_i is the number of voxels of the ith chalcopyrite grain.

Additionally, we calculate the pore and chalcopyrite/sulfur grain size distribution and their changes across three stages. This is done on the images after per-grain/pore isolation using the "regionprop3" function in MATLAB. The size of each pore/grain is represented by the equivalent diameter, which is the diameter of a sphere with the same volume as the object.

2.4.2. Fluid-Accessible Specific Surface Area

Lastly, fluid-accessible specific surface area (fluid-accessible SSA) refers to the specific surface area (SSA) exposed to the pore space where reactions occur. It is characterized by two parameters: the liberation ratio and the SSA. The liberation ratio is determined by extracting the outer boundary of each 3D grain and calculating the ratio of the voxels that represent pore space to the total voxels at the outer boundary. The detailed procedure for calculating the liberation ratio is as follows:

- The outer boundary of each 3D grain is extracted using the "circshift" function in MATLAB. This function performs a circular shift on a 2D slice, considering connectivity with 8 neighboring voxels. The bounding box of each grain is first extracted and then padded by one voxel of zero value in each dimension. After that, every

slice along the X-Y plane in the bounding box is processed using the "circshift" function. By processing all the slices along the *Z*-axis, the outer boundary is identified.

- The number of voxels on the outer boundary that belong to the pore phase is calculated. The liberation ratio is then determined by the ratio of the voxels that represent pore space to the total voxels at the outer boundary.

SSA is defined as the ratio between the surface area and the mass of the grain. The surface area of each grain is determined from images after per-grain isolation using the "regionprop3" function in MATLAB. For mass calculation, the whole sample contains 0.2 g of chalcopyrite, and the overall voxel count for the chalcopyrite phase is determined during three-phase segmentation. Using these two data sets, the mass per voxel for the chalcopyrite phase can be calculated. The grain mass is then obtained by multiplying the mass per voxel by the number of voxels corresponding to each grain. The fluid-accessible surface area of grains is then calculated by multiplying the liberation ratio by the surface area and the fluid-accessible SSA of grains is calculated by multiplying the liberation ratio by the SSA. At each stage, the fluid-accessible SSA is determined for every grain, allowing for the determination of a time-dependent fluid-accessible SSA.

Notably, image resolution is a crucial factor that affects the surface characterization accuracy. Higher resolution provides a more detailed representation of phase boundaries, capturing finer surface morphologies and resulting in more accurate SSA measurements. In contrast, lower resolution leads to voxelation effects, where complex surfaces appear artificially smoothed due to the limited number of voxels. This can result in an underestimation or overestimation of the true SSA during image segmentation. In our case, the sample is made of only two minerals with a distinct density difference, and the chalcopyrite grain size used to create the sample is much larger than the voxel resolution (80 μm compared to 4 μm). Therefore, the image resolution should be sufficient to capture the chalcopyrite grain and its grain morphologies in the sample. Meanwhile, the highest resolution that can be achieved with the micro-CT scanner is highly related to the sample diameter. Given the diameter of our sample, we have scanned it at the highest voxel resolution achievable with our micro-CT system to ensure a correct image-based SSA characterization.

2.4.3. Geochemical Modeling Using Phreeqc

Phreeqc (V3.7.3) is a widely used geochemical software for various subsurface applications (Zeng et al., 2022; Zhang et al., 2019), including chalcopyrite dissolution (Y. Li et al., 2015). In this study, we developed a Phreeqc model that is tailored for chalcopyrite grains and the consolidated chalcopyrite sample based on the reaction rate law provided in Kimball et al. (2010). The chalcopyrite dissolution rate (*mole/s*) is modeled in Phreeqc RATES module exactly as

$$R_{\text{Chalcopyrite}} = -A(t)a_{\text{Experiment}}^n r_{\text{Chalcopyrite}} \tag{10}$$

where the $A(t)$ is the linear time function of chalcopyrite fluid-accessible surface area (cm^2), defined as:

$$A(t) = A_0 + \frac{A_{\text{end}} - A_0}{t_{\text{end}} - t_0}(t - t_0) \tag{11}$$

where t is the simulation time (s), A_0 is the fluid-accessible surface area of chalcopyrite (grain or the whole sample, cm^2) at the initial simulation time (e.g., initial stage of the experiment), A_{end} is the fluid-accessible surface area of chalcopyrite at the end of simulation time (cm^2), t_0 and t_{end} are the initial and end of the simulation time, respectively. Noted that our objective is to assess the impact of incorporating time-dependent surface area measurements from images on geochemical simulation results by comparing them with simulations that only use a constant surface area for each grain. A linear interpolation (Equation 11) is selected as an example to estimate surface area values between two stages for all grains. Investigating any more complex dissolution models is not the main focus here. In Equation 10, $a_{\text{Experiment}}^n$ is a single parameter that represents the product of all the far from equilibrium effects on the reaction of the specific experiment, for example, catalytic effects Steefel et al. (2015). This number is used because geochemical reactions are inherently complex and could be affected by many factors. A single parameter $a_{\text{Experiment}}^n$ is thus defined to represent all such factors. $r_{\text{Chalcopyrite}}$ is the chalcopyrite dissolution rate law in the presence of Fe^{3+} provided by (Kimball et al., 2010) as

19447973, 2025, 7, Downloaded from https://agupubs.onlinelibrary.wiley.com/doi/10.1029/2024WR039414 by Technical University Delft, Wiley Online Library on [09/07/2025]. See the Terms and Conditions (https://onlinelibrary.wiley.com/terms-and-conditions) on Wiley Online Library for rules of use; OA articles are governed by the applicable Creative Commons License

$$r_{\text{Chalcopyrite}} = 10^{1.88} e^{-48100/RT} [H^+][Fe^{3+}]^{0.42} \qquad (12)$$

where the $[H^+]$ and Fe^{3+} are the solution activities of hydrogen and iron ions, respectively.

For Phreeqc simulations of each chalcopyrite grain and the whole sample, our image-based fluid-accessible surface area and initial moles of chalcopyrite are input into the PHASES module of Phreeqc, which is the module used to define thermodynamic properties and reaction equations for minerals and other phases. During the simulation, the total moles of the chalcopyrite that dissolve are recorded and compared with the amount of dissolution quantified from micro-CT images. All the simulations are performed under a synthetic database which integrates the databases of *phreeqc* and *wateq*4*f*, while excluding all the species that are not present in our system.

In Phreeqc simulation studies, a constant initial mineral SSA is typically maintained throughout the entire simulation process (Awolayo et al., 2022; Bo et al., 2021; Zeng et al., 2022). However, as demonstrated in this study and (Qin et al., 2023), the fluid-accessible mineral SSA evolves dynamically during dissolution and precipitation. To highlight the importance of incorporating a time-dependent fluid-accessible surface area in our model (Equations 10 and 11), we conducted an additional set of simulations using the same input parameters as before. In these simulations, however, the parameter *t* in Equation 11 was set to 0, effectively assuming a constant fluid-accessible surface area. Table S3 in Supporting Information S1 provides an overview of the chalcopyrite and surface area input of each Phreeqc simulation case.

3. Results

3.1. Experimental Copper Recovery Through Electrokinetic

The chalcopyrite powder used to create the sample is tested using XRD and XRF analysis to confirm the mineral and elemental compositions, as summarized in Table S4 in Supporting Information S1. From the analysis, we can see that the powder consists of a substantial amount of chalcopyrite, with only minor amounts of other Fe- and Cu-bearing minerals (such as pyrite and azurite) and gangue minerals (such as quartz and anorthoclase).

The core-scale experiment, conducted using a series of reservoirs, aims to understand mineral dissolution and precipitation under EK conditions (Figure 2c). $FeCl_3$ (0.5 M) solution is used as the lixiviant in reservoir II. An external constant electric potential (7.5 V) is applied, leading to the electromigration of charged ions. The amount of Cu^{2+} and Fe^{3+} recovered at reservoir IV is measured by ICP-MS, as shown in Figures 4a and 4b. The amount of Cu^{2+} recovered increases dramatically during the first 200 hr, stabilizes in the next 800 hr, and then declines to a minimal recovery rate in the final 200 hr. According to the ICP-MS results, approximately 12.1 mg of Cu^{2+} is recovered in the first 200 hr. This amount increases to 16.9 mg after 1,000 hr and eventually reaches 17.2 mg of Cu^{2+}. For the Fe^{3+}, as shown in Figure 4b, at reservoir II (inlet), with the transport of Fe^{3+} toward the cathode, the amount of Fe^{3+} reduces. This value goes back to 560 mg every time after refreshing the lixiviant in reservoir II. The fluid in reservoir IV is also refreshed after sampling. Reservoirs II and IV are refreshed with 0.5 M $FeCl_3$ in 0.2 M HCl and 0.3 M NaCl in 0.2 M HCl, respectively. Another reason for refreshing reservoirs II and IV is to ensure an acidic condition (i.e., pH < 2) to maintain solubility of the Fe^{3+} and avoid any precipitation of $Fe(OH)_3$. pH values in reservoirs II and IV are regularly measured (<1) (Figure 4c). Consequently, no precipitation of $Fe(OH)_3$ occurs during the experiment. The voltages in the different reservoirs level off after 2 hr (Figure 4d). The stabilized voltage across the sample is around 1.2 V (II–IV, the blue line in Figure 4d). The voltage gradient is around 0.6 V/cm, which is a reasonable voltage gradient compared to other EK subsurface applications, such as EK soil remediation (Kim et al., 2011; Mena et al., 2016).

3.2. Time-Lapse Micro-CT Image Visualization and Processing Results

Figure 5 displays the time-lapse micro-CT images captured at three stages: the initial stage before the experiment, the middle stage after 500 hr of leaching, and the final stage after 1,200 hr of leaching. Figure 5a presents the volume rendering of the sample from the micro-CT images at three stages, while Figure 5b specifically illustrates the 3D distribution of chalcopyrite at these stages extracted from segmented images. The volume of chalcopyrite substantially decreases from the initial to the middle stage, with only slight changes observed by the final stage. This image-based observation aligns with the experimental results, where a substantial amount of Cu ions is
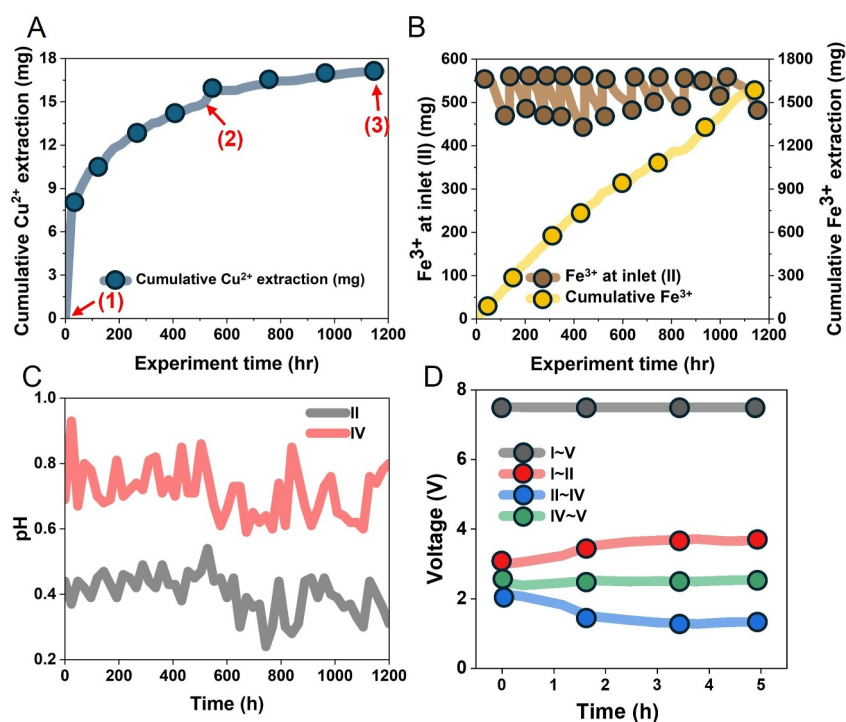
Figure 4. Experimental results: (a) Cumulative mass extraction of Cu^{2+}. The sample was also scanned using micro-CT at three intervals: step (1) at 0 hr, step (2) at 500 hr, and step (3) at 1,200 hr. (b) Mass of injected Fe^{3+} at inlet and cumulative Fe^{3+} extracted at outlet. (c) Recorded pH values in reservoirs II and IV. (d) Recorded voltage between different reservoirs.

extracted from the initial to the middle stage. In Figures 5c and 5d, a clearer comparison is provided through a 2D segmented slice and its magnified regions in the X-Z plane of the sample, showing how chalcopyrite grains either disappear or shrink under the influence of the electric field. Figure S2 (Supporting Information S1) gives an example of the three-phase segmentation results and pre-grain isolation results at three stages. From the grayscale micro-CT image (Figure S2 in Supporting Information S1, first row), the brighter voxels represent the chalcopyrite phase as the chalcopyrite has a higher density compared to glass beads and pore space.

We also conduct a sensitivity analysis of the three-phase segmentation to assess how the segmentation is affected by varying watershed threshold values. This involves selecting a series of threshold ranges for watershed segmentation and calculating the differences in the chalcopyrite phase compared to the threshold range used in the manuscript. The quantified differences at three stages are shown in Figure S3 in Supporting Information S1. As the threshold range gradually increases, the differences grow across all three stages. However, these differences remain relatively small, ranging from 1% to 6%, indicating that the segmentation of the sample is not sensitive to the change of threshold range. This is because the grayscale distributions of pore, glass beads, and chalcopyrite are well-separated from each other due to the significant density differences between these phases. The change of threshold range would only influence very limited number of voxels at the phase boundary. Meanwhile, the per-grain isolation images (Figure S2 in Supporting Information S1 bottom row) label each chalcopyrite grain as a separate instance, assigning a unique label to all the corresponding voxels. In total, 138,614, 87,600, and 57,205 chalcopyrite grains are obtained for the initial, middle, and final stages, respectively.

3.3. Ion Transport Analysis

Ion transport is analyzed using the EDI and ADI values calculated from the experimental setting and the effective diffusivity based on the numerical simulation of 3D images. Firstly, several driving mechanisms exist for ion transport in a reactive transport system, including advection, diffusion, and electromigration. In our experiment, we applied only an external electric field, without the application of external pressure. The fluid flows extremely slowly under electroosmosis (Tang, Li, et al., 2023), resulting in a low advective flux of ions. Consequently, the ADI value is close to zero, indicating that ion transport is primarily governed by electromigration and diffusion.
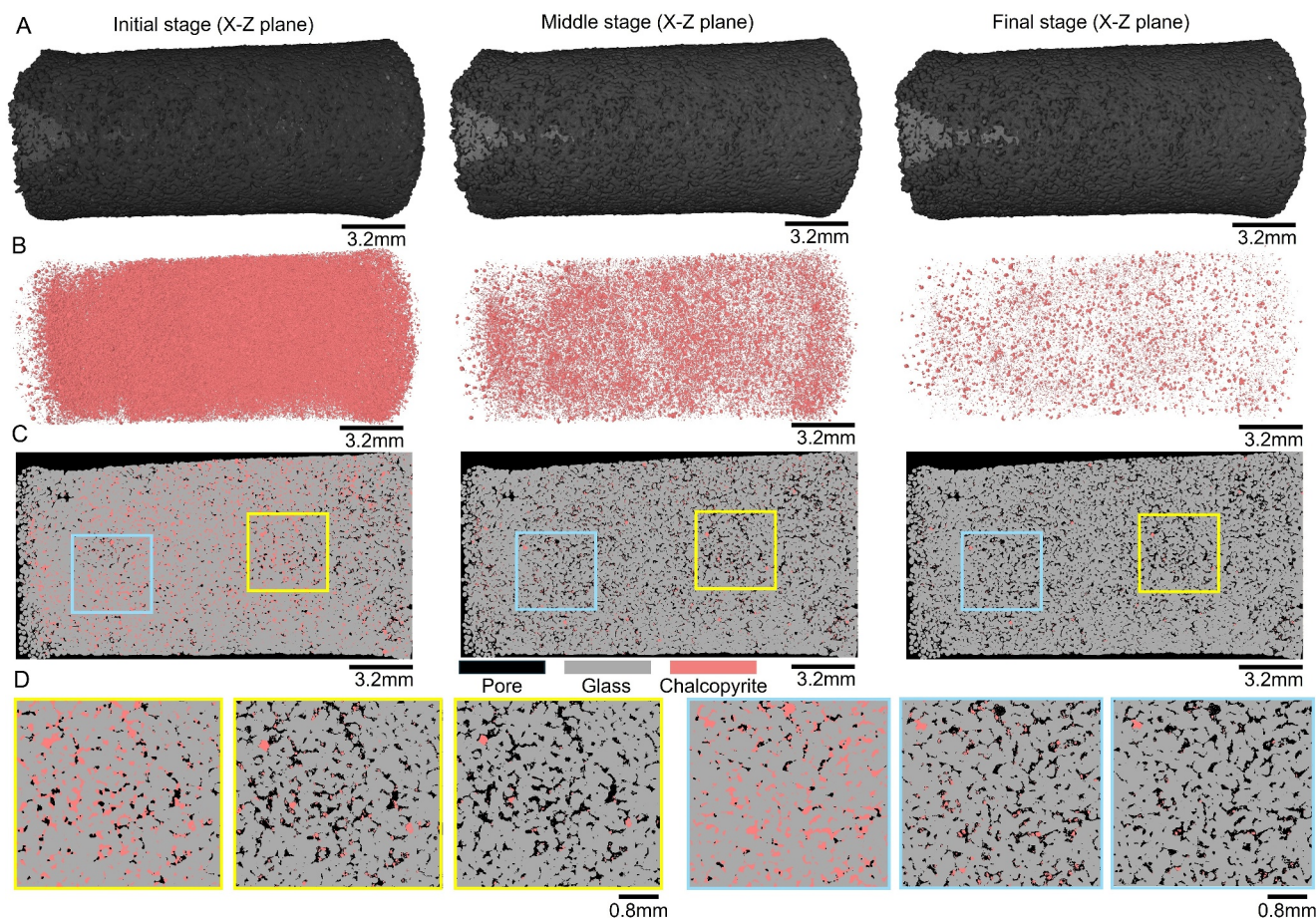
Figure 5. Visualization of the sample and the segmentation results across three stages. (a) 3D rendering of the 3D micro-CT image of the sample. (b) Highlighted chalcopyrite phase from the segmented images. (c) 2D example of the three-phase segmentation results. (d) Magnified regions on the 2D segmented slices. In the yellow and blue highlighted box, the left: Initial stage; middle: Middle stage; right: Final stage.

To determine the EDI value, we estimate the experimental parameters for ferric ions, as they are the main reactive ions interacting with chalcopyrite. The calculated EDI is around 70 (experimental parameters for calculating EDI are listed in Table S5 in Supporting Information S1). According to the ion transport diagram reported in Tang et al. (2024) (as shown in Figure 6), depending on different ADI and EDI values, ions exhibit four transport regimes, including large channeling, small channeling, uniform transport, and no transport. Accordingly, the ion transport regime with an EDI of 70 and an ADI close to 0 should be uniform transport. Under uniform transport, ions move uniformly into the sample and transport through both large and small connected pores. The uniform transport behavior is further confirmed in Figure 8b, which shows the change in the volume fraction of chalcopyrite at three stages across each 2D slice along the main transport direction. A uniform decrease in chalcopyrite volume fraction can be observed in each slice from the initial stage to the middle stage and then to the final stage, indicating uniform ion transport into the sample.

To provide insights into the impact of tortuosity and porosity changes during mineral dissolution and precipitation on ion transport, a diffusion simulation is then performed directly on a subset 3D domain ($1,351 \times 1,151 \times 3,881$ voxels) (Figure 7a) cropped from the entire volumes ($2,119 \times 2,113 \times 4,066$ voxels) at three stages. Initially, the connected path is limited from the inlet to the outlet due to the low porosity. As porosity increases to 0.122 and 0.141 in the middle and final stages (Figure 7b), the simulated effective diffusivity rises to 0.0017 and then doubles to 0.0032, indicating that the ions can transport more easily through the sample. As shown in Figures 7c and 7d, the dissolution of chalcopyrite leads to an increase in porosity and prompts the formation of additional ion transport pathways for diffusive flux. During the middle stage, only a few connected paths exit near the sample's inlet, whereas a greater number of connected paths appear in the central region. In the final stage, as chalcopyrite
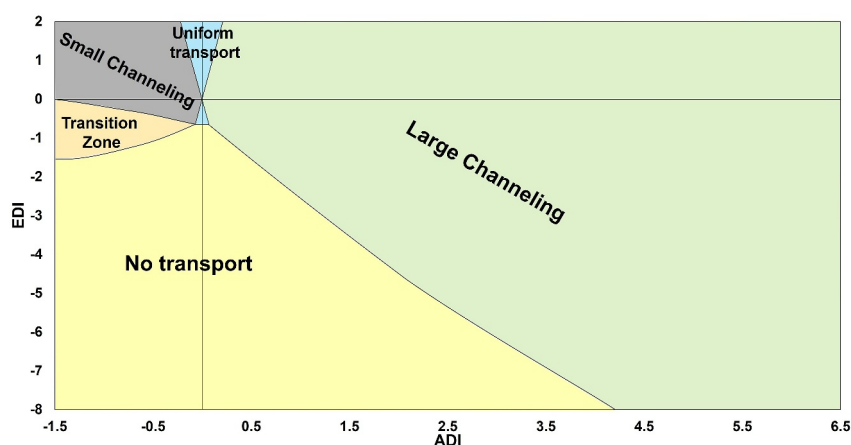
Figure 6. Illustration of the ion transport diagram based on the ADI and EDI numbers (Tang et al., 2024). In the experimental system, the ADI is close to zero, while the EDI is approximately 70, indicating uniform ion transport throughout the sample.

grains dissolve, more continuous paths form between the inlet and outlet. The following sections will present a detailed analysis of chalcopyrite dissolution, secondary precipitation, and their influence on the formation and interconnection of connected pathways.

3.4. Chalcopyrite Dissolution Analysis

After examining the transport behavior of the reactive ion, we characterize the dissolution process of chalcopyrite based on images and validate the results through geochemical reaction simulation using Phreeqc. A detailed characterization result of the dissolution process is shown in Figure 8. The decrease of chalcopyrite grain (dissolution) voxel frequency and the increase of pore voxel frequency are notable from the initial to the middle stage (the first 500 experimental hours). However, as shown in Figure 8a, these changes become less substantial from the middle stage to the final stage (the subsequent 700 experimental hours). Based on the image analysis, the recovery of chalcopyrite is 53.1% at the middle stage and 78.7% at the final stage.

Figure 8b, as previously mentioned, confirms that the ion transport and dissolution are uniform. The per-grain basis calculation results are shown in Figures 8c–8f. As displayed by the histogram charts in Figure 8c, the chalcopyrite grains shrink, transitioning leftward (toward a smaller diameter) from the initial stage to the final stage. Meanwhile, the decrease in grain frequency in Figure 8c indicates that many grains have completely dissolved (138,614 at the initial stage compared to 57,205 at the final stage). To further compare the dissolution of
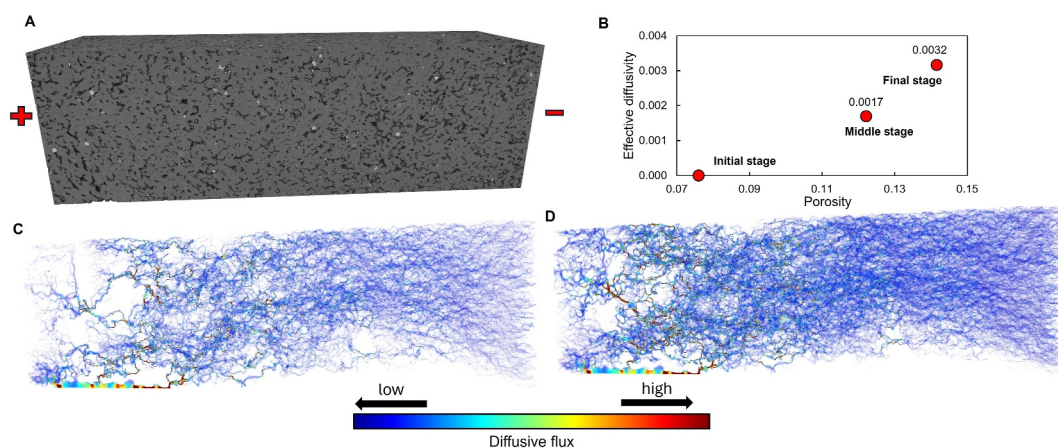

Figure 7. Diffusion simulation of the middle stage and final stage. (a) 3D rendering 3D micro-CT domain used for simulation. (b) Effective diffusion coefficient versus porosity at three stages. (c) Diffusive flux field for the middle stage. (d) Diffusive flux field for the final stage.
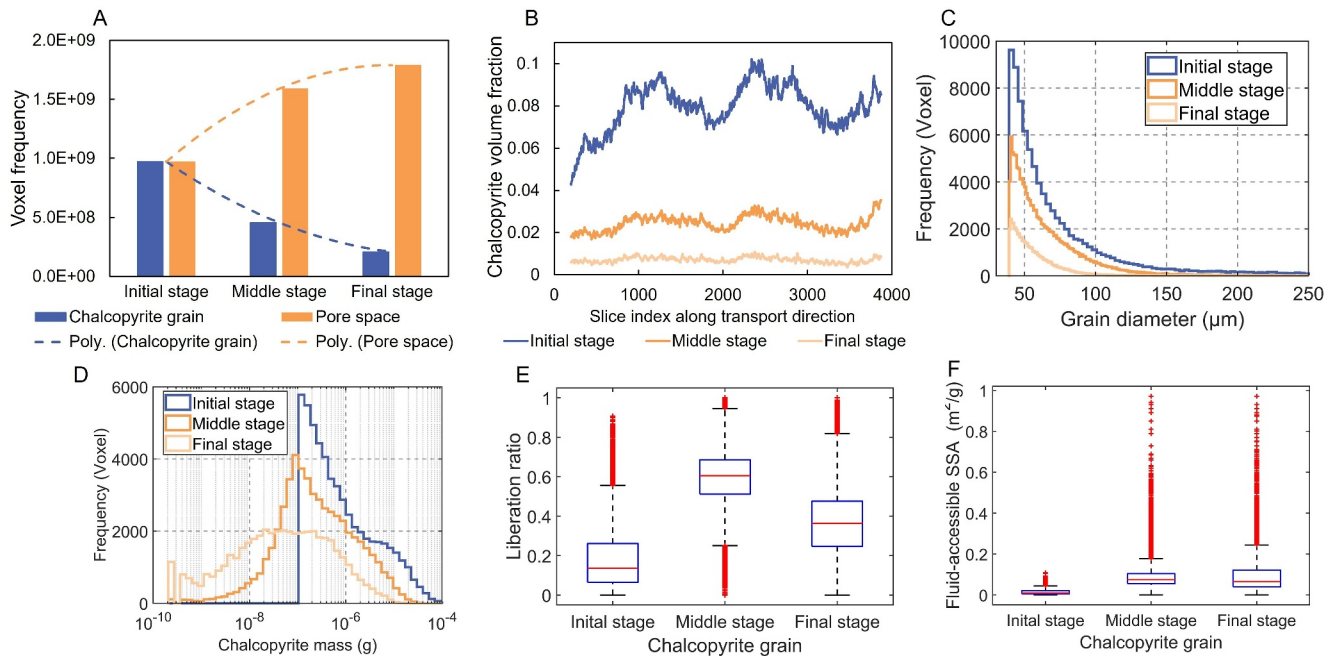
Figure 8. Image-based dissolution analysis results. (a) Voxel frequency changes across three stages. (b) Chalcopyrite volume fraction at each 2D slice along the main transport direction. (c) Chalcopyrite grain size distribution at three stages. (d) Mass of the Chalcopyrite grain and the distribution. (e) Liberation ratio of each chalcopyrite grain at three stages. (f) Fluid-accessible SSA of each chalcopyrite grain at three stages.

grains in terms of mass, liberation ratio, and fluid-accessible SSA across three stages, we select grains that are not fully dissolved at the final stage, and their voxel numbers are still enough for calculating meaningful physical parameters. With this, a total of 54,380 chalcopyrite grains are selected and tracked at three stages. Figure 8d shows the weight reduction of these 54,380 grains from the initial stage to the final stage. Liberation ratio and fluid-accessible SSA are two essential parameters that influence the dissolution process.

Figures 8e and 8f shows the liberation ratio and fluid-accessible SSA distribution of these 54,380 chalcopyrite grains in a boxplot. The bottom and top of the blue box are the first and third quartiles of the data, and the red line in the middle of each blue box is the median point. The whiskers are the dashed lines extending from the box, representing the range of data within 1.5 times the interquartile range from the quartiles. Any data points outside the whiskers are considered outliers (shown as red points), indicating that these points are significantly different from the rest of the data.

At the initial stage, the majority of the grain's surface is not liberated and is not exposed to the pore, with the median liberation ratio being approximately only 0.13 (13% of the surface is exposed to the pore space). Consequently, the fluid-accessible SSA is also low at this stage, with the median value around 0.01 m^2/g. The outliers, which are mainly located above the maximum whisker point for both liberation ratio and fluid-accessible SSA, suggest that a few grains are already well-liberated in the initial stage.

In the middle stage, both the liberation ratio and the fluid-accessible SSA increase, reaching median values of 0.6 and 0.08, respectively. This indicates that most parts of the chalcopyrite grains are liberated, allowing the grain surface to be in effective contact with the reactive ions. A notable increase in the outlier values for the fluid-accessible SSA suggests that some grains are highly well-liberated at this stage. However, the outliers for the liberation ratio, primarily located below the minimum whisker point, indicate that a few grains remain poorly liberated at this stage.

In the final stage, the median values of both the liberation ratio and the fluid-accessible SSA decrease. This suggests that well-liberated grains have already dissolved, while for partially liberated grains, the liberated part is also dissolved. Additionally, a few newly liberated grains can be observed from the outliers in the final stage. These outliers are mainly located above the maximum whisker point, indicating that these grains have a high
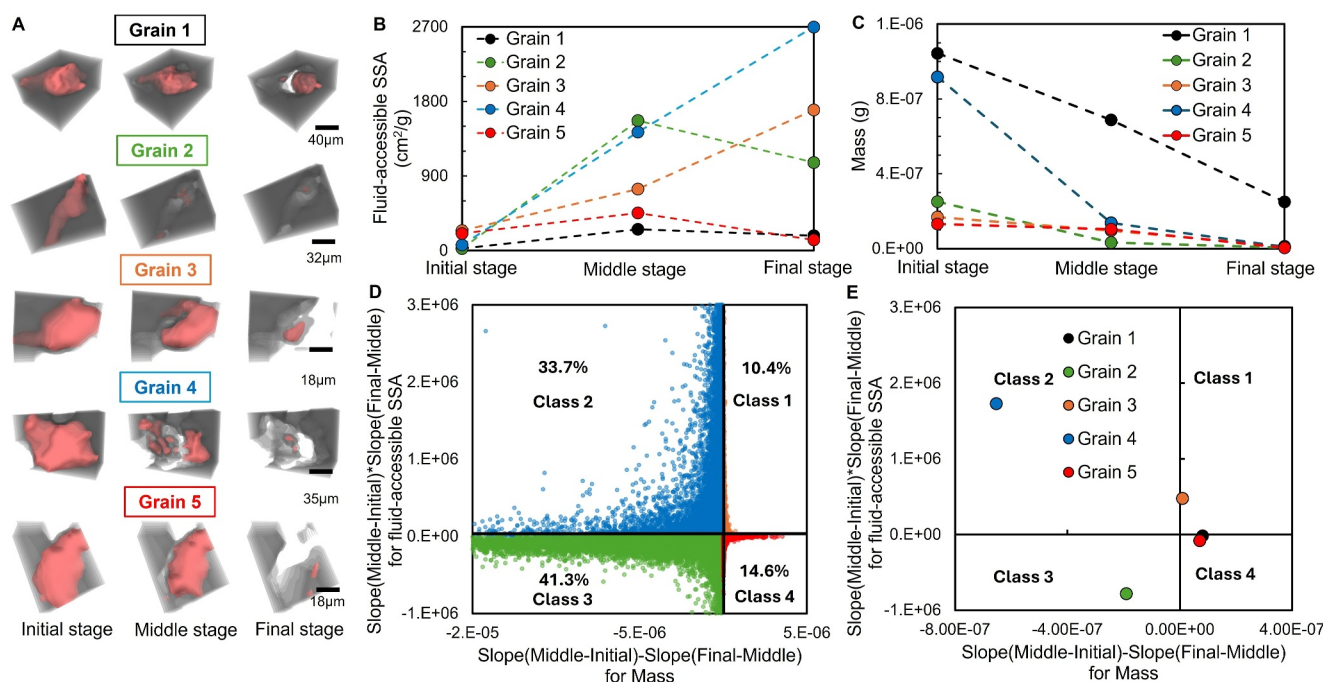
Figure 9. (a) 3D visualization of chalcopyrite grains during dissolution across three stages for five grains. (b) Scatter plots depicting fluid-accessible specific surface area (SSA) at each of the three stages. (c) Scatter plots illustrating grain mass across the three stages. (d) Slope analysis of fluid-accessible SSA and grain mass for 54,380 grains. The *X*-axis represents the difference in the slope of grain mass from the initial to the middle stage and from the middle to the final stage. The *Y*-axis represents the product of the slopes for fluid-accessible SSA from the initial to the middle stage and from the middle to the final stage. Four distinct dissolution behaviors are identified for all grains, corresponding to the four quadrants of the scatter plot. (e) Classes of the five example grains based on the classification criteria in (d).

liberation ratio and fluid-accessible SSA even at the final stage. These newly liberated grains are likely the ones that were poorly liberated during the previous stages.

To further illustrate the complex dissolution pattern of chalcopyrite grains at different stages, five chalcopyrite grains with distinct dissolution behaviors are selected and plotted in 3D (Figure 9a), along with their fluid-accessible SSA and mass at three stages (Figures 9b and 9c). Their liberation ratio across three stages is provided in Figure S4 in Supporting Information S1. Given that there is a time difference between reactive ions reaching chalcopyrite grains at the different sections of the sample during the experiment and this will affect the dissolution process, these five grains are located in the same section of the sample near the inlet. Grain 1 and Grain 5 show an extremely low fluid-accessible SSA before the dissolution (initial stage) because the grain is surrounded by glass beads, as shown in Figure 9a. As the mineral grain dissolves and shrinks, a fraction of the grain surface will detach with surrounding glass beads and provide more space and flow path for ions to penetrate the grain, leading to an increased fluid-accessible SSA in the middle stage and a strong dissolution of the mass afterward. The fluid-accessible SSA decreases from here till the final stage because most of the grain has been dissolved. Grain 3 exhibits a similar dissolution behavior to Grain 1 and Grain 5 from the initial stage to the middle stage. However, from the middle stage to the final stage, Grain 3 shows a completely different behavior: the fluid-accessible SSA increases dramatically due to the higher liberation ratio (Figure S4 in Supporting Information S1).

For Grain 2 and Grain 4, as shown in Figure 9a, the dissolution of Grain 2 primarily occurs from the initial stage to the middle stage, during which most of the volume is dissolved. Two potential reasons behind this are: (a) despite all the selected grains being located in the nearby section of the sample, the ion transport paths can still vary notably. As a result, Grain 2 comes into contact with ions earlier than the others; (b) Grain 2 has a stripe shape compared to other grains, which are mostly spherical-like shapes. This distinctive morphology can result in a sudden increase in the liberation ratio due to its higher surface-to-volume ratio, leading to rapid dissolution occurring at an earlier stage, which our images did not capture. Finally, for Grain 4, the fluid-accessible SSA increases from 66 to 1,430 and 2,700 cm^2/g at three stages with an extremely high liberation ratio (around 0.8).

This shows very different behavior from other grains. While others only shrink as a whole during dissolution, Grain 4 breaks down into many sub-grains. This fragmentation increases the liberation ratio and surface area, resulting in a strong dissolution of Grain 4 throughout all three stages.

Overall, four distinct dissolution behaviors are observed, with the primary features summarized below:

- *Class 1* (e.g., Grains 3): From the initial to middle stage, grain dissolution occurs steadily, leading to an increase in both fluid-accessible SSA and liberation ratio. From the middle to the final stage, the fluid-accessible SSA increases significantly, and a high liberation ratio is maintained. This suggests that with the dissolution, more ions are able to interact with the grain.
- *Class 2* (e.g., Grains 4): Grain dissolution primarily occurs at an earlier stage. However, unlike class 1, where the grain only shrinks as a whole during dissolution, this type of grain breaks apart into multiple sub-grains. Consequently, the fluid-accessible SSA increases substantially, allowing a high liberation ratio to be maintained.
- *Class 3* (e.g., Grains 2): Grain dissolution primarily occurs at an earlier stage. In the later stage, the volume of the grain becomes small. Thus, the fluid-accessible SSA and liberation ratio are reduced.
- *Class 4* (e.g., Grains 1 and 5): Grain dissolution is steady due to the low fluid-accessible SSA that limits the reaction. Although fluid-accessible SSA is low, it gradually transitions from an unliberated form at the early stage to a more liberated form, resulting in a greater fluid-accessible SSA. However, as the dissolution proceeds, less fluid can get access to the grain due to the smaller grain volume, and fluid-accessible SSA drops back.

Based on the primary features of these classes, we define classification criteria for these grains based on the slope of fluid-accessible SSA and grain mass across three stages. We calculate the slopes for fluid-accessible SSA and grain mass between the initial and middle stages and the period between the middle and final stages. The slope of fluid-accessible SSA could serve as a proxy for surface morphology evolution dynamics. A positive slope suggests an increase in fluid-accessible surface area, either due to the exposure of new reaction sites or the formation of pores and cracks. In contrast, a negative slope indicates a reduction in accessible surface area, which may result from the loss of liberated sites as the reaction progresses or passivation caused by sulfur precipitation. Meanwhile, the slope of mass could serve as a proxy for the local effective reaction rate. A higher slope indicates a faster dissolution rate, suggesting either rapid surface reaction kinetics or enhanced reactive ion accessibility. In contrast, a lower slope indicates a reduced reaction rate, potentially due to surface passivation, a decrease in liberated reactive surfaces, or a local depletion of reactive ions near the mineral surface. The detailed classification criteria are obtained as follows:

- Firstly, we calculated the fluid-accessible SSA and mass for all 54,380 chalcopyrite grains at three stages. Three measured points for fluid-accessible SSA and mass at three stages are then connected with a linear line (as an example shown in Figures 9b and 9c).
- After that, the mass of chalcopyrite grains consistently decreases from the initial to the middle and final stages due to dissolution. As a result, only two possible dissolution classes can be extrapolated from the mass measurements at three stages: (a) rapid dissolution from the initial to the middle stage, followed by slower dissolution from the middle to the final stage (such as Grains 2 and 4); and (b) slow dissolution from the initial to the middle stage, followed by faster dissolution from the middle to the final stage (such as Grains 1, 3, and 5). The dissolution rate can be effectively quantified using the slope of the line. By subtracting the slope from the initial to the middle stage from the slope of the middle to the final stage, a positive result indicates class (1), while a negative result indicates class (2).
- Meanwhile, for fluid-accessible SSA, all grains exhibit an increase in value from the initial to the middle stage. However, from the middle to the final stage, both increases and decreases in fluid-accessible SSA are observed. Consequently, two distinct dissolution classes can be inferred from the fluid-accessible SSA measurements across the three stages: (a) a positive slope from the initial to the middle stage, which remains positive from the middle to the final stage (such as Grains 3 and 4); and (b) a positive slope from the initial to the middle stage, which then becomes negative from the middle to the final stage (such as Grains 1, 2 and 5).
- By combining the extrapolated classes from mass and fluid-accessible SSA measurements, an overall of 4 classes can be defined for these 54,380 grains.

Based on these observations, we multiply the slope from the initial to the middle stage by the slope from the middle to the final stage of the fluid-accessible SSA. Meanwhile, for the grain mass, we subtract the slope from the initial to
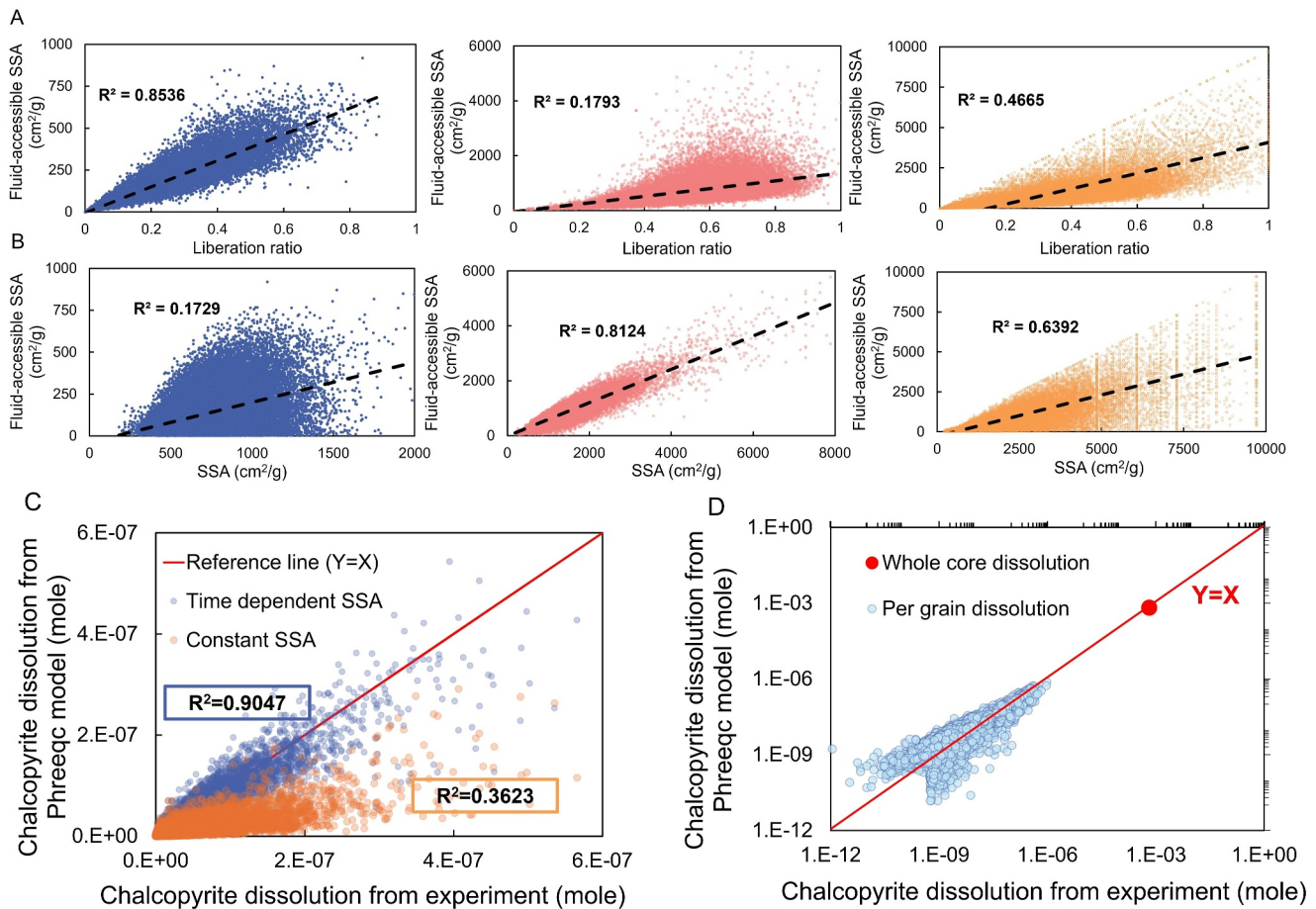
Figure 10. Scatter plot of (a) per-grain fluid-accessible SSA with the liberation ratio, dash line represents the linear relationship for R^2; (b) per-grain fluid-accessible SSA with the SSA, dash line represents the linear relationship for R^2; (c) per-grain chalcopyrite dissolution of Phreeqc model prediction using time-dependent (blue points) or constant (orange points) fluid-accessible SSA with the dissolution of experimental image-based observation; (d) per-grain (light blue points) and core-scale (red point) chalcopyrite dissolution of Phreeqc model prediction with the dissolution of experimental image-based observation.

the middle stage from the slope from the middle to the final stage. Finally, we apply the classification criteria to all grains based on their mass and fluid-accessible SSA values at the initial, middle, and final stages. These 54,380 grains are successfully classified into these four classes (Figure 9d). The four quadrants correspond to the four distinct classes, with a fraction of 10.4% for class 1, 33.7% for class 2, 41.3% for class 3%, and 14.6% for class 4. Classes 2 and 4 are the predominant dissolution classes, suggesting that most grains can be liberated and well-connected by reactive ions. This also implies that grain dissolution primarily occurs at an earlier stage, which aligns with our experimental observations. The classes of the five example grains are also plotted in Figure 9e.

These dissolution behaviors from selected grains explain the coefficient of determination $\left(R^2\right)$ between our image-based fluid-accessible SSA with the liberation ratio (Figure 10a) and the SSA (Figure 10b) at the three stages. As discussed previously, at the initial stage, most of the chalcopyrite grain surface is not liberated, resulting in fluid-accessible SSA ranging from several to only hundreds of cm^2/g. The smaller fluid-accessible SSA at this stage means it is mainly determined by the liberation ratio ($R^2 = 0.85$, left figure of Figure 10a) and shows a weak relationship with the SSA ($R^2 = 0.17$, left figure of Figure 10b). With the dissolution proceeds, more mineral surface starts to be detached and liberated from the surrounding glass beads. During the middle stage of this process, the SSA of the chalcopyrite grains significantly influences the fluid-accessible SSA $\left(R^2 = 0.81\right)$, while the liberation ratio shows little impact ($R^2 = 0.18$, the middle figure of Figures 10a and 10b). Compared to the correlation observed in the initial stage, which is primarily dominated by the liberation ratio, and the middle stage, where SSA plays a more significant role, the final stage exhibits a mixed control mechanism, where both factors influence dissolution, but neither shows a clear dominant correlation with fluid-accessible SSA.

We also compared our image-based measured SSA with BET-measured SSA for chalcopyrite reported from literature Acero et al. (2009), J. Li et al. (2010), and Y. Li et al. (2015), Specifically, previous studies have reported BET surface areas for chalcopyrite minerals as follows: 2,000 to 2,800 cm^2/g in Y. Li et al. (2015), 6,230 cm^2/g in J. Li et al. (2010), and 7,000 to 7,200 cm^2/gin Acero et al. (2009). For our image-based measurements, as shown in Figure 10b, the SSA for most chalcopyrite grains ranges from 200 to 1,500 cm^2/g at the initial stage. In the middle stage, SSA values extend up to 5,000 cm^2/g, with most values between 1,000 and 4,000 cm^2/g. At the final stage, SSA increases further, reaching up to 10,000 cm^2/g, with most values falling between 2,500 and 6,000 cm^2/g. Compared to literature values, our image-based SSA measurements at the initial stage are lower than the reported BET surface areas. However, as the leaching process progresses, in the middle and the final stages, the SSA values obtained from our image-based analysis become more comparable to the BET surface area range.

Our Phreeqc chalcopyrite dissolution predictions further validate our image-based chalcopyrite characterizations. For the Phreeqc simulation, we assume that the input chalcopyrite fully contacts and reacts with a 0.5 M FeCl$_3$ solution (pH = 0.56) from the beginning of the simulation. This assumption is supported by the ion transport characterization in Section 3.3 where the inlet ions uniformly transport into the system under electromigration and diffusion. Figure 10c presents a scatter plot of per-grain Phreeqc chalcopyrite dissolution prediction results, comparing time-dependent (blue points) and constant (orange points) fluid-accessible SSA, and their correlation with image-based experimental measurements at the middle stage. Predictions considering the fluid-accessible SSA variation during the dissolution process show a strong agreement with our image-based experimental chalcopyrite dissolution observations $\left(R^2 = 0.90\right)$. In contrast, applying a constant fluid-accessible SSA (using the fluid-accessible SSA at the initial stage) in Phreeqc modeling would lead to a significant discrepancy compared to our experimental results $\left(R^2 = 0.36\right)$. Moreover, the model prediction using the core-scale input (see Table S3 in Supporting Information S1) also agrees with the experiment result with 1% (percentage of the experiment result) error, shown in Figure 10d. These results illustrate the accuracy and robustness of our image-based mineral dissolution characterization workflow, as it can capture the mineral dissolution behaviors across scales and perform better than the conventional method.

3.5. Elemental Sulfur Precipitation Analysis

The chemical reaction system of our experiment reveals the possibility of elemental sulfur precipitation. The following section presents our image-based analysis of the elemental sulfur precipitation. The elemental sulfur has a density of around 2–2.2 g/cm^3 (Meyer, 1976; Shuai & Meisen, 1995), glass beads of around 2.4 g/cm^3, and chalcopyrite of around 4.3 g/cm^3 (Burdick & Ellis, 1917), respectively. In micro-CT images, chalcopyrite will exhibit the highest grayscale values due to its high density, followed by glass beads and elemental sulfur. Glass beads and elemental sulfur have similar densities. As a result, they will display similar grayscale values in the micro-CT images, making visual identification challenging. However, since no reaction will occur with the glass beads and no hydraulic pressure is applied, their structure will remain unchanged across the three stages. Therefore, the elemental sulfur precipitation can be identified by checking the differences in the glass bead phase between the three stages. The detailed elemental sulfur identification and segmentation process can be found in Supporting Information S1.

The sulfur precipitation, as shown in Figures 11a and 11b, is represented by difference maps between the initial stage and the middle stage, and between the initial stage and the final stage, respectively. By visual inspection, we can see that precipitated sulfur exists in the sample at both stages, and there is more in the middle stage than in the final stage. Figure 11c shows the voxel frequency of elemental sulfur across 2D slices from inlet to outlet, and we found that precipitation happens more at the middle stage than at the final stage. There are two possible reasons for this:

- The first factor contributing to sulfur reduction in the final stage is the migration of sulfur grains. As chalcopyrite dissolves, the sample's porosity increases, creating more connected flow paths. Meanwhile, given the large time interval between the middle stage and the final stage (700 hr), along with the applied electric field and the surface charge of the minerals, the fluid phase is moved toward outlet reservoir IV through electroosmosis, carrying some of the sulfur grains out of the sample. Sulfur migration with electroosmotic flow can be evidenced in Figure S7A in Supporting Information S1. Specifically, the red box in Figure S7A in
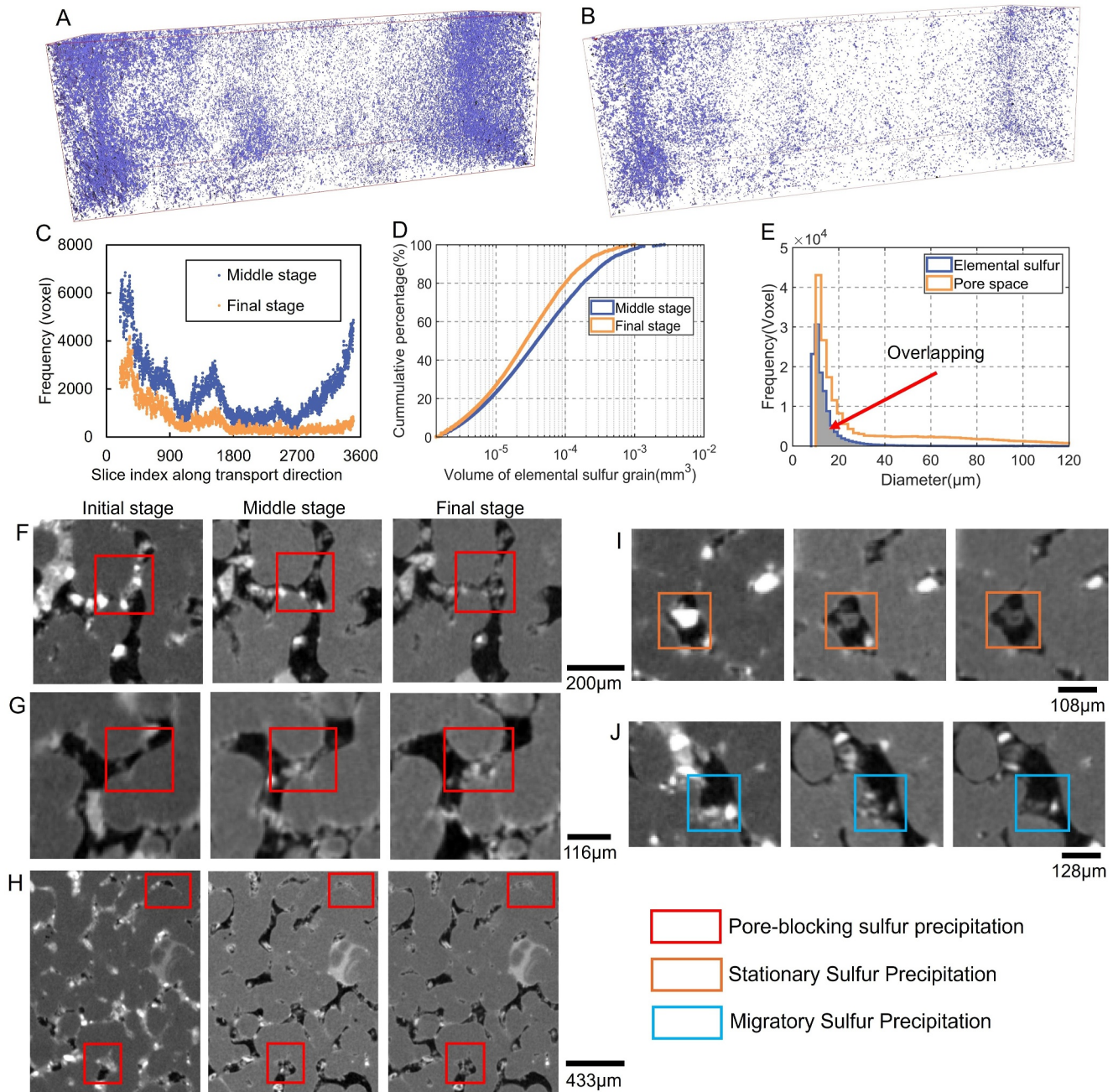
Figure 11. Quantification of the elemental sulfur precipitation and visualization of elemental sulfur precipitation from micro-CT images. (a) 3D rendering of the sulfur precipitation at the middle stage. (b) 3D rendering of the sulfur precipitation at the final stage. (c) Voxel frequency of sulfur around 2D slices from the inlet to the outlet of the sample. (d) Cumulative percentage of the volume for the elemental sulfur. (e) Elemental sulfur grain size distribution and the pore size distribution at the middle stage. (f)–(h) Examples of pore-blocking sulfur precipitation. (i) Examples of stationary precipitation. (j) Examples of migratory sulfur precipitation.

Supporting Information S1 highlights precipitates moving out of the sample. Additionally, the water level difference between reservoirs II and IV confirms the presence of electroosmotic flow, which transports the fluid phase from reservoir II to reservoir IV.

- Secondly, a secondary reaction occurs that dissolves the elemental sulfur. The secondary reaction under strong acidic conditions would be (Breuker & Schippers, 2024; Brock & Gustafson, 1976):

$$S^0 + 6Fe^{3+} + 4H_2O \rightarrow HSO_4^- + 6Fe^{2+} + 7H^+ \tag{13}$$
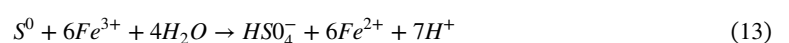
This occurs because, during the later stages of the experiment (from the middle to the final stage), the chalcopyrite mass decreases significantly, while the Fe^{3+} concentration remains high due to the periodic refreshing of inlet reservoir II. Consequently, the available Fe^{3+} can react with elemental sulfur, leading to the dissolution of the elemental sulfur. The secondary reaction that dissolves the elemental sulfur can be evidenced in Figure S7B in Supporting Information S1. Specifically, Figure S7B in Supporting Information S1 is taken after Figure S7A in Supporting Information S1. The precipitates in the red box of Figure S7A in Supporting Information S1 have disappeared in Figure S7B in Supporting Information S1. This dissolution occurs due to the presence of Fe^{3+} in reservoir IV and the acidic conditions.

Meanwhile, a large amount of precipitation near the inlet and a noticeable absence of sulfur precipitation in the middle can be observed. This is likely due to three reasons: (a) the rate of dissolution was higher near the inlet, leading to larger concentration gradients that further promoted precipitation; (b) at the inlet, while a significant number of sulfur grains precipitate, the interconnected pathways leading to the middle section are highly limited, with most pore spaces remaining disconnected from the outlet. This is evidenced by the diffusion simulation in Figures 7b and 7c. These limited percolating paths captured in the diffusion simulation allow very limited free sulfur grains to move to the middle part, while most of the sulfur grains would be trapped as the stationary sulfur precipitation in the inlet part; and (c) as observed in the diffusion simulation (Figures 7b and 7c), numerous interconnected pathways form in the middle section of the sample. Consequently, any sulfur grains that precipitate in this region or were moved previously from the inlet part can be easily migrated to the outlet by electroosmotic flow.

Figure 11d shows the volume cumulative percentage of elemental sulfur grains at the middle stage and final stage, and we find that the elemental sulfur grain volume is larger in the middle stage than in the final stage. Figure 11e compares the sulfur grain size distribution with the pore size distribution at the middle stage. An overlapping region is observed between the two distributions, indicating that the size of the elemental sulfur is comparable to the pore size. Consequently, there is a possibility that large sulfur grains can block small pores, thereby impacting geochemical reactions and ion transport. This is further confirmed in Figures 11f–11j, which shows five examples of precipitation in the grayscale images at three stages. Figures 11f–11h shows the precipitation of sulfur grains, which block the pore space, particularly at the pore throats where the size is smaller than the pore bodies. We name this type of precipitation "pore-blocking sulfur precipitation." Apart from it, two more types of sulfur precipitation are observed, as shown in Figures 11i and 11j. In Figure 11i, the chalcopyrite grain dissolved with a sulfur grain precipitated at the same location, remaining intact until the final stage. We name this type of precipitation "stationary sulfur precipitation." Lastly, in Figure 11j, after the dissolution of the chalcopyrite grain, sulfur precipitation forms in the middle stage. However, this precipitated sulfur disappears in the final stage, likely due to being moved by electroosmosis or undergoing a secondary reaction. We name this type of precipitation "migratory sulfur precipitation." A 2D visual example of the segmented sulfur precipitates is also given in Figure S8 in Supporting Information S1, which shows the 2D difference map between the initial, middle, and final stages. The colored boxes highlight these defined sulfur types: precipitation pore-blocking sulfur precipitation (red box), stationary sulfur precipitation (green and blue boxes), and migratory sulfur precipitation (yellow box).

4. Discussion

Geochemical reactive transport modeling can potentially resolve the longstanding issue of laboratory-field rate discrepancy in the geochemical literature (Steefel, 2019). Many efforts have been made to capture the core-scale mineral dissolution behavior through mineral surface area measurement (Awolayo et al., 2022; Battu et al., 2024; Beckingham et al., 2016). Whereas, the core-scale mineral surface area characterization method presented in the literature still suffers from the inability to deal with the smaller-scale mineral heterogeneity (Qin et al., 2023). However, as shown in our ion diffusion simulation, such pore-scale heterogeneity varies significantly during geochemical reactive processes. An oversight on this would lead to discrepancies between modeling and the actual results (Awolayo et al., 2022; Qin et al., 2023). In this context, we propose an image-based pore-scale mineral dissolution and precipitation characterization workflow to investigate the complex dissolution and precipitation behaviors of chalcopyrite during EK-ISR operation. Four dissolution patterns and three precipitation patterns (*Pore-blocking*, *Stationary Sulfur*, and *Migratory Sulfur* precipitation) are found, with each leading to distinct mineral fluid-accessible SSA and influences on core-scale accessibility, porosity, and associated

geochemical reaction dynamics. These findings explain the potential issues with the previous mineral surface area characterization and modeling methods in the literature (Awolayo et al., 2022; Beckingham et al., 2016; Bo et al., 2021; Zeng et al., 2022) where constant BET values or 2D fluid-accessible SSA are used. For example, in Awolayo et al. (2022), although a reasonably good match between the continuum core-scale reactive transport simulation and the experiment results was achieved, there were still some mismatches for the effluent concentration and the permeability changes. These discrepancies have been attributed to the inability to handle some transient fluid-rock interaction processes and the formation of preferential flow paths due to dissolution by the end of the experiment. Our study shows that the proposed workflow can capture and model these complex dissolution and precipitation processes by characterizing time-lapse 3D pore-scale parameters such as the fluid-accessible SSA. As shown in Figures 9a and 9b, the 3D geometry of each chalcopyrite grain does not vary linearly in time-scale along the experiment process, with a greater complexity during the middle to final stage compared to the period between the initial and middle stages. These observations are consistent with the results presented in Awolayo et al. (2022) and Qin et al. (2023), showcasing the potential of our workflow to resolve issues with proper implementation.

The alignment of the core-scale chalcopyrite dissolution with the pore-scale results (Figure 10d), achieved by using the total fluid-accessible SSA of each chalcopyrite grain at the pore scale, demonstrates that the proposed workflow enables the upscaling of pore-scale findings to the core scale, allowing for the prediction of core-scale dissolution. Accurate mineral dissolution and precipitation prediction at any scale would only be achieved when all these time-dependent statuses are well-captured and described through the geochemical reaction models and added up. Although the geochemical reaction model presented in this study achieves a strong agreement with image-based experimental observation by considering linear time-dependent chalcopyrite fluid-accessible SSA, applying this model to grains with varying dissolution behaviors could be insufficient. This also explains why the R^2 in Figure 10c and D are not approaching 1. Moreover, the grain-wise chalcopyrite fluid-accessible SSA and mass are calculated based on a synthetic core sample, a more advanced method, for example, the one presented in Tang et al. (2022) would be needed to calculate these parameters from a real core sample. Therefore, further work may include investigating the correct way to model these factors not only in the context of EK-chalcopyrite mineral recovery context but also in other geochemical systems (e.g., CCS) with a real ore sample.

5. Conclusions

A thorough experimental and time-lapse 3D image-based workflow is presented to characterize the reactive transport process of mineral dissolution and precipitation at the pore-core scale. This workflow is specifically applied to investigate ion transport, chalcopyrite dissolution, and elemental sulfur precipitation under an EK-ISR process. The main research findings can be summarized as follows.

1. By calculating two ion transport-related dimensionless numbers (EDI and ADI), uniform ion transport is predicted based on the theoretical ion transport regime (Tang et al., 2024). Experimental results and 3D micro-CT images confirm this, showing uniform chalcopyrite dissolution across the sample over 1,200 hr, aligning with theoretical predictions.
2. Cross-comparison of time-lapse micro-CT images of all chalcopyrite grains at three stages reveals complex dissolution behaviors. Four distinct dissolution patterns are identified, each affecting the chalcopyrite dissolution rate. The fluid-accessible SSA, crucial in geochemical modeling, is initially influenced by the liberation ratio and later by the SSA. These relationships weaken in the final dissolution stage.
3. The chalcopyrite dissolution predictions using our developed Phreeqc model with the per-grain time-dependent fluid-accessible SSA agree with both grain and core-scale experimental image-based results $(R^2 = 0.9048)$ while the same model with constant surface area input would result in an R^2 of 0.3623.
4. Elemental sulfur precipitation is evident in the images. Three distinct precipitation patterns are identified and illustrated, such as pore-blocking sulfur precipitation, which is crucial for reactive transport systems as it obstructs the pore space and therefore influences the ion transport pathway.

Overall, we systematically characterize the time-dependent complexities of mineral dissolution and precipitation during the EK-ISR process. Further analysis highlights the importance of accurately modeling these behaviors for optimizing EK-ISR operations from pore to core scale. Taken together, the workflow has the potential to be applied to other geosystems (e.g., CCS) to characterize transport, dissolution, and precipitation.

Data Availability Statement

Data related to chalcopyrite characterization from micro-CT images and phreeqcRC simulation results are available via Tang (2024). Diffusion simulation code is also available at Tang (2024).

References

Acero, P., Cama, J., Ayora, C., & Asta, M. (2009). Chalcopyrite dissolution rate law from pH 1 to 3. *Geológica Acta*, *7*(3), 389–397.

Al-Yaseri, A., Fatah, A., Alsaif, B., Sakthivel, S., Amao, A., Al-Qasim, A. S., & Yousef, A. A. (2024). Subsurface hydrogen storage in limestone rocks: Evaluation of geochemical reactions and gas generation potential. *Energy & Fuels*, *38*(11), 9923–9932. https://doi.org/10.1021/acs.energyfuels.4c00742

Antonijević, M., & Bogdanović, G. (2004). Investigation of the leaching of chalcopyritic ore in acidic solutions. *Hydrometallurgy*, *73*(3–4), 245–256. https://doi.org/10.1016/j.hydromet.2003.11.003

Awolayo, A. N., Laureijs, C. T., Byng, J., Luhmann, A. J., Lauer, R., & Tutolo, B. M. (2022). Mineral surface area accessibility and sensitivity constraints on carbon mineralization in basaltic aquifers. *Geochimica et Cosmochimica Acta*, *334*, 293–315. https://doi.org/10.1016/j.gca.2022.08.011

Battu, A. K., Miller, Q. R., Cao, R., Owen, A. T., & Schaef, H. T. (2024). 3d quantification of pore networks and anthropogenic carbon mineralization in stacked basalt reservoirs. *Environmental Science & Technology*, *58*(8), 3747–3754. https://doi.org/10.1021/acs.est.3c06163

Beckingham, L. E., Mitnick, E. H., Steefel, C. I., Zhang, S., Voltolini, M., Swift, A. M., et al. (2016). Evaluation of mineral reactive surface area estimates for prediction of reactivity of a multi-mineral sediment. *Geochimica et Cosmochimica Acta*, *188*, 310–329. https://doi.org/10.1016/j.gca.2016.05.040

Ben-Awuah, E., Richter, O., Elkington, T., & Pourrahimian, Y. (2016). Strategic mining options optimization: Open pit mining, underground mining or both. *International Journal of Mining Science and Technology*, *26*(6), 1065–1071. https://doi.org/10.1016/j.ijmst.2016.09.015

Bennett, C., McBride, D., Cross, M., & Gebhardt, J. (2012). A comprehensive model for copper sulphide heap leaching: Part 1 basic formulation and validation through column test simulation. *Hydrometallurgy*, *127*, 150–161.

Beucher, S., & Meyer, F. (2018). The morphological approach to segmentation: The watershed transformation. In *Mathematical morphology in image processing* (pp. 433–481). CRC Press.

Bo, Z., Zeng, L., Chen, Y., & Xie, Q. (2021). Geochemical reactions-induced hydrogen loss during underground hydrogen storage in sandstone reservoirs. *International Journal of Hydrogen Energy*, *46*(38), 19998–20009. https://doi.org/10.1016/j.ijhydene.2021.03.116

Breuker, A., & Schippers, A. (2024). Rates of iron (III) reduction coupled to elemental sulfur or tetrathionate oxidation by acidophilic microorganisms and detection of sulfur intermediates. *Research in Microbiology*, *175*(1–2), 104110. https://doi.org/10.1016/j.resmic.2023.104110

Brock, T. D., & Gustafson, J. (1976). Ferric iron reduction by sulfur-and iron-oxidizing bacteria. *Applied and Environmental Microbiology*, *32*(4), 567–571. https://doi.org/10.1128/aem.32.4.567-571.1976

Burdick, C. L., & Ellis, J. H. (1917). The crystal structure of chalcopyrite determined by x-rays. *Journal of the American Chemical Society*, *39*(12), 2518–2525. https://doi.org/10.1021/ja02257a002

Chung, T., Wang, Y. D., Armstrong, R. T., & Mostaghimi, P. (2019). Approximating permeability of microcomputed-tomography images using elliptic flow equations. *SPE Journal*, *24*(3), 1154–1163. https://doi.org/10.2118/191379-pa

Dutrizac, J. (1990). Elemental sulphur formation during the ferric chloride leaching of chalcopyrite. *Hydrometallurgy*, *23*(2–3), 153–176. https://doi.org/10.1016/0304-386x(90)90002-j

Guo, J.-T., Wei, Y.-Q., Chen, S.-L., Sun, W., Fan, T.-T., Xu, M.-R., & Zhang, C.-C. (2022). Measurement of pore diffusion factor of porous solid materials. *Petroleum Science*, *19*(4), 1897–1904. https://doi.org/10.1016/j.petsci.2022.04.008

Hellerschmied, C., Schritter, J., Waldmann, N., Zaduryan, A. B., Rachbauer, L., Scherr, K. E., et al. (2024). Hydrogen storage and geo-methanation in a depleted underground hydrocarbon reservoir. *Nature Energy*, *9*(3), 333–344. https://doi.org/10.1038/s41560-024-01458-1

Hiroyoshi, N., Arai, M., Miki, H., Tsunekawa, M., & Hirajima, T. (2002). A new reaction model for the catalytic effect of silver ions on chalcopyrite leaching in sulfuric acid solutions. *Hydrometallurgy*, *63*(3), 257–267. https://doi.org/10.1016/s0304-386x(01)00228-6

Holditch, S. A. (2013). Unconventional oil and gas resource development–let's do it right. *Journal of Unconventional Oil and Gas Resources*, *1*, 2–8. https://doi.org/10.1016/j.juogr.2013.05.001

Kanakiya, S., Adam, L., Esteban, L., Rowe, M. C., & Shane, P. (2017). Dissolution and secondary mineral precipitation in basalts due to reactions with carbonic acid. *Journal of Geophysical Research: Solid Earth*, *122*(6), 4312–4327. https://doi.org/10.1002/2017jb014019

Karami, E., Kuhar, L., Bona, A., & Nikoloski, A. N. (2021). A review of electrokinetic, ultrasonic and solution pulsing methods for mass transfer enhancement in in-situ processing. *Minerals Engineering*, *170*, 107029. https://doi.org/10.1016/j.mineng.2021.107029

Karami, E., Kuhar, L., Bona, A., & Nikoloski, A. N. (2023). Investigation of the effect of different parameters on lixiviant ion migration in a laboratory scale study of electrokinetic in-situ recovery. *Mineral Processing and Extractive Metallurgy Review*, *44*(1), 1–12. https://doi.org/10.1080/08827508.2021.2017924

Khajooie, S., Gaus, G., Dohrmann, A. B., Krüger, M., & Littke, R. (2024). Methanogenic conversion of hydrogen to methane in reservoir rocks: An experimental study of microbial activity in water-filled pore space. *International Journal of Hydrogen Energy*, *50*, 272–290. https://doi.org/10.1016/j.ijhydene.2023.07.065

Kim, G.-N., Shon, D.-B., Park, H.-M., Lee, K.-W., & Chung, U.-S. (2011). Development of pilot-scale electrokinetic remediation technology for uranium removal. *Separation and Purification Technology*, *80*(1), 67–72. https://doi.org/10.1016/j.seppur.2011.04.009

Kimball, B. E., Rimstidt, J. D., & Brantley, S. L. (2010). Chalcopyrite dissolution rate laws. *Applied Geochemistry*, *25*(7), 972–983. https://doi.org/10.1016/j.apgeochem.2010.03.010

Krevor, S., De Coninck, H., Gasda, S. E., Ghaleigh, N. S., de Gooyert, V., Hajibeygi, H., et al. (2023). Subsurface carbon dioxide and hydrogen storage for a sustainable energy future. *Nature Reviews Earth & Environment*, *4*(2), 102–118. https://doi.org/10.1038/s43017-022-00376-8

Kuhar, L. L., Breuer, P. L., Haque, N., & Robinson, D. J. (2018). Considerations and potential economic advantages for the in-situ recovery of gold from deep, hard-rock deposits. *Minerals Engineering*, *121*, 14–22. https://doi.org/10.1016/j.mineng.2018.02.026

Kumar, K. R., Honorio, H., Chandra, D., Lesueur, M., & Hajibeygi, H. (2023). Comprehensive review of geomechanics of underground hydrogen storage in depleted reservoirs and salt caverns. *Journal of Energy Storage*, *73*, 108912. https://doi.org/10.1016/j.est.2023.108912

Lasaga, A. C. (1981). Transition state theory. *Reviews in Mineralogy*, *8*.

Li, J., Kawashima, N., Kaplun, K., Absolon, V., & Gerson, A. (2010). Chalcopyrite leaching: The rate controlling factors. *Geochimica et Cosmochimica Acta*, *74*(10), 2881–2893. https://doi.org/10.1016/j.gca.2010.02.029

Li, Y., Qian, G., Li, J., & Gerson, A. R. (2015). Kinetics and roles of solution and surface species of chalcopyrite dissolution at 650 mv. *Geochimica et Cosmochimica Acta*, *161*, 188–202. https://doi.org/10.1016/j.gca.2015.04.012

Maitland, G. (2000). Oil and gas production. *Current Opinion in Colloid & Interface Science*, *5*(5–6), 301–311. https://doi.org/10.1016/s1359-0294(00)00069-8

Martens, E., Prommer, H., Sprocati, R., Sun, J., Dai, X., Crane, R., et al. (2021a). Toward a more sustainable mining future with electrokinetic in situ leaching. *Science Advances*, *7*(18), eabf9971. https://doi.org/10.1126/sciadv.abf9971

Martens, E., Prommer, H., Sprocati, R., Sun, J., Dai, X., Crane, R., et al. (2021b). Toward a more sustainable mining future with electrokinetic in situ leaching. *Science Advances*, *7*(18), eabf9971. https://doi.org/10.1126/sciadv.abf9971

Marty, N. C., Claret, F., Lassin, A., Tremosa, J., Blanc, P., Madé, B., et al. (2015). A database of dissolution and precipitation rates for clay-rocks minerals. *Applied Geochemistry*, *55*, 108–118. https://doi.org/10.1016/j.apgeochem.2014.10.012

Mena, E., Villaseñor, J., Rodrigo, M. A., & Cañizares, P. (2016). Electrokinetic remediation of soil polluted with insoluble organics using biological permeable reactive barriers: Effect of periodic polarity reversal and voltage gradient. *Chemical Engineering Journal*, *299*, 30–36. https://doi.org/10.1016/j.cej.2016.04.049

Menefee, A. H., Li, P., Giammar, D. E., & Ellis, B. R. (2017). Roles of transport limitations and mineral heterogeneity in carbonation of fractured basalts. *Environmental Science & Technology*, *51*(16), 9352–9362. https://doi.org/10.1021/acs.est.7b00326

Meyer, B. (1976). The structures of elemental sulfur. *Advances in Inorganic Chemistry and Radiochemistry*, *18*, 287–317. https://doi.org/10.1016/s0065-2792(08)60032-1

Mudd, G. M. (2001). Critical review of acid in situ leach uranium mining: 1. USA and Australia. *Environmental Geology*, *41*(3–4), 390–403. https://doi.org/10.1007/s002540100406

Palandri, J. L., & Kharaka, Y. K. (2004). *A compilation of rate parameters of water-mineral interaction kinetics for application to geochemical modeling* Technical report. US Geological Survey.

Qin, F., Salek, M. F., Asadi, P., & Beckingham, L. E. (2023). Evolution of mineral-accessible surface area induced by geochemical reactions. *ACS Earth and Space Chemistry*, *7*(4), 753–763. https://doi.org/10.1021/acsearthspacechem.2c00335

Salomons, W. (1995). Environmental impact of metals derived from mining activities: Processes, predictions, prevention. *Journal of Geochemical Exploration*, *52*(1–2), 5–23. https://doi.org/10.1016/0375-6742(94)00039-e

Sandve, T. H., Berre, I., & Nordbotten, J. M. (2012). An efficient multi-point flux approximation method for discrete fracture–matrix simulations. *Journal of Computational Physics*, *231*(9), 3784–3800. https://doi.org/10.1016/j.jcp.2012.01.023

Seredkin, M., Zabolotsky, A., & Jeffress, G. (2016). In situ recovery, an alternative to conventional methods of mining: Exploration, resource estimation, environmental issues, project evaluation and economics. *Ore Geology Reviews*, *79*, 500–514. https://doi.org/10.1016/j.oregeorev.2016.06.016

Shojaee, A., Ghanbari, S., Wang, G., & Mackay, E. (2024). Interplay between microbial activity and geochemical reactions during underground hydrogen storage in a seawater-rich formation. *International Journal of Hydrogen Energy*, *50*, 1529–1541. https://doi.org/10.1016/j.ijhydene.2023.10.061

Shuai, X., & Meisen, A. (1995). New correlations predict physical properties of element sulfur. *Oil & Gas Journal*, *93*(42), 50–55.

Sinclair, L., & Thompson, J. (2015). In situ leaching of copper: Challenges and future prospects. *Hydrometallurgy*, *157*, 306–324. https://doi.org/10.1016/j.hydromet.2015.08.022

Steefel, C. I. (2019). Reactive transport at the crossroads. *Reviews in Mineralogy and Geochemistry*, *85*(1), 1–26. https://doi.org/10.2138/rmg.2019.85.1

Steefel, C. I., Appelo, C. A. J., Arora, B., Jacques, D., Kalbacher, T., Kolditz, O., et al. (2015). Reactive transport codes for subsurface environmental simulation. *Computational Geosciences*, *19*(3), 445–478. https://doi.org/10.1007/s10596-014-9443-x

Tang, K. (2024). Per-chalcopyrite particle morphological analysis data obtaining from three time-lapse micro-ct images and the phreeqcrm simulation data [Dataset]. *Zenodo*. https://doi.org/10.5281/zenodo.15239075

Tang, K., Bo, Z., Li, Z., Da Wang, Y., McClure, J., Su, H., et al. (2024). Controlled ion transport in the subsurface: A coupled advection–diffusion–electromigration system. *Physics of Fluids*, *36*(6). https://doi.org/10.1063/5.0213161

Tang, K., Da Wang, Y., Mostaghimi, P., Knackstedt, M., Hargrave, C., & Armstrong, R. T. (2022). Deep convolutional neural network for 3d mineral identification and liberation analysis. *Minerals Engineering*, *183*, 107592. https://doi.org/10.1016/j.mineng.2022.107592

Tang, K., Da Wang, Y., Niu, Y., Honeyands, T. A., O'Dea, D., Mostaghimi, P., et al. (2023). Particle classification of iron ore sinter green bed mixtures by 3d x-ray microcomputed tomography and machine learning. *Powder Technology*, *415*, 118151. https://doi.org/10.1016/j.powtec.2022.118151

Tang, K., Li, Z., Da Wang, Y., McClure, J., Su, H., Mostaghimi, P., & Armstrong, R. T. (2023). A pore-scale model for electrokinetic in situ recovery of copper: The influence of mineral occurrence, zeta potential, and electric potential. *Transport in Porous Media*, 1–26.

Tarkowski, R. (2019). Underground hydrogen storage: Characteristics and prospects. *Renewable and Sustainable Energy Reviews*, *105*, 86–94. https://doi.org/10.1016/j.rser.2019.01.051

Tremosa, J., Jakobsen, R., & Le Gallo, Y. (2023). Assessing and modeling hydrogen reactivity in underground hydrogen storage: A review and models simulating the lobodice town gas storage. *Frontiers in Energy Research*, *11*, 1145978. https://doi.org/10.3389/fenrg.2023.1145978

Wang, G., Xu, J., Ran, L., Zhu, R., Ling, B., Liang, X., et al. (2022). A green and efficient technology to recover rare earth elements from weathering crusts. *Nature Sustainability*, *6*, 1–12. https://doi.org/10.1038/s41893-022-00989-3

Wang, G., Xu, J., Ran, L., Zhu, R., Ling, B., Liang, X., et al. (2023). A green and efficient technology to recover rare Earth elements from weathering crusts. *Nature Sustainability*, *6*(1), 81–92. https://doi.org/10.1038/s41893-022-00989-3

Xiaoguang, T., Zhang, G., Zhaoming, W., Zhixin, W., Zuoji, T., Hongjun, W., et al. (2018). Distribution and potential of global oil and gas resources. *Petroleum Exploration and Development*, *45*(4), 779–789. https://doi.org/10.1016/s1876-3804(18)30081-8

Zeng, L., Keshavarz, A., Xie, Q., & Iglauer, S. (2022). Hydrogen storage in majiagou carbonate reservoir in China: Geochemical modelling on carbonate dissolution and hydrogen loss. *International Journal of Hydrogen Energy*, *47*(59), 24861–24870. https://doi.org/10.1016/j.ijhydene.2022.05.247

Zhang, Y., Hu, B., Teng, Y., Tu, K., & Zhu, C. (2019). A library of basic scripts of reaction rates for geochemical modeling using phreeqc. *Computers & Geosciences*, *133*, 104316. https://doi.org/10.1016/j.cageo.2019.104316